

See discussions, stats, and author profiles for this publication at: <https://www.researchgate.net/publication/224924544>

Electronic Spectroscopy and Computational Studies of Glutathionylco(III)balamin

ARTICLE *in* THE JOURNAL OF PHYSICAL CHEMISTRY A · MAY 2012

Impact Factor: 2.69 · DOI: 10.1021/jp301294x · Source: PubMed

CITATIONS

3

READS

34

4 AUTHORS, INCLUDING:



Azaria S Eisenberg

New York University

5 PUBLICATIONS 6 CITATIONS

[SEE PROFILE](#)



Vasilii S Znamenskiy

City University of New York - Borough of Manh...

11 PUBLICATIONS 362 CITATIONS

[SEE PROFILE](#)



Ronald L Birke

City College of New York

91 PUBLICATIONS 2,997 CITATIONS

[SEE PROFILE](#)

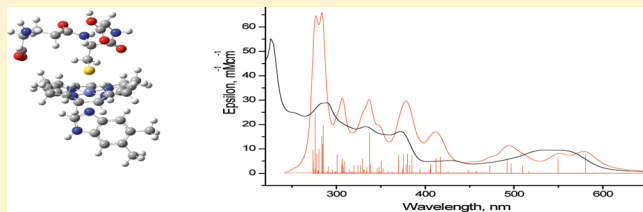
Electronic Spectroscopy and Computational Studies of Glutathionylco(III)balamin

Azaria S. Eisenberg, Iya V. Likhtina, Vasiliy S. Znamenskiy, and Ronald L. Birke*

Department of Chemistry, The City College of New York, and The Graduate School and University Center, The City University of New York, New York, New York 10031, United States

 Supporting Information

ABSTRACT: We have studied glutathionylcobalamin (GS-Cbl) by optical spectroscopy and with density functional theory (DFT) and time-dependent DFT (TD-DFT) electronic structure methods of truncated geometric models. We examined the geometric structure of the models by comparison of DFT calculations with recent high-resolution experimental X-ray structure data (Hannibal, L. et al. *Inorg. Chem.* 2010, 49, 9921) for GS-Cbl, and we examined the TD-DFT excitation simulations by comparison of the models with measured optical spectra. The calculations employed the B3LYP hybrid functional and the nonhybrid BP86 functional in both vacuum and water (conductor polarized continuum model (cpcm)) with the 6-311G(d,p) basis set. The optimized geometric structure calculations for six truncated models were made by varying the chemical structure, solvent model, and the two DFT functionals. All showed similar geometry. Charge decomposition analysis (CDA) and extended charge decomposition analysis (ECDA), especially with BP86 shows the similar charge transfer nature of the Co–S bond in GS-Cbl and the Co–C bond in CH₃Cbl. Mayer and Wiberg bond orders illustrate the similar covalent nature of the two bonds. Finally, absolute optical spectral simulation calculations were compared with the experimental UV–visible extinction spectrum and the electronic circular dichroism (ECD) differential extinction spectrum. The BP86 method shows more spectral features, and the best fit was found for a GS-Cbl model with 5,6-dimethylbenzimidazole at the BP86/6-311G(d,p) level with a water cpcm solvent model. The excited state transitions were investigated with Martin’s natural transition orbitals (NTOs). The BP86 calculations also showed π bonding interactions between Co and the axial S of the GS-ligand in the molecular orbitals (MOs) and NTOs.



I. INTRODUCTION

Alkylcorrinoids function as cofactors in a number of mammalian and prokaryotic enzyme systems, the most well studied being the cobalamin (Cbl)-dependent enzymes with cofactors of methylco(III)balamin (Me-Cbl(III)) and adenosylco(III)balamin (Ado-Cbl(III)), the so-called coenzymes of vitamin B₁₂. These cofactors contain a cobalt–carbon bond that is cleaved during the enzymatic reaction and are found in humans in the B₁₂-dependent enzymes: methionine synthase (MetH), which binds Me-Cbl, and methylmalonyl-coenzyme A mutase (MMCA), which binds Ado-Cbl. On the other hand, the tripeptide γ -glutamylcysteinylglycine or glutathione (GSH) is a major intracellular reducing agent present in almost all biological tissues and acts to mitigate oxidative stress. The thiolato derivatives of cobalamins were first investigated in 1964¹ and 1966.² Jacobsen and co-workers in a series of studies³ considered glutathionylcob(III)alamin (GS-Cbl(III)) to be a natural precursor to the two cobalamin coenzymes, and they also considered it likely that GS-Cbl(III) is the predominant form of vitamin B₁₂ in mammalian cells.⁴

Reports by Brasch, Finke, and co-workers⁵ show that glutathionylcobalamin (GS-Cbl) has a unique stability in comparison with other thiolatocobalamins. Considering the fact that GSH is present in most biological tissues at much

higher concentration (1–10 mM)⁶ than cobalamin and that it has a high binding affinity for replacing H₂O in H₂O-Cbl(III)⁺,^{7c} GS-Cbl(III) may well be the reservoir for cob(III)alamin in mammalian biological systems. This evidence suggests that GS-Cbl(III) is an important intermediate for biological processes involving vitamin B₁₂ species.

The structural chemistry of GS-Cbl has been well studied including NMR spectra,⁷ X-ray analysis by extended X-ray absorption fine structure (EXAFS) giving Co–N and Co–S bond distances,⁸ and, more recently, complete structures by X-ray diffraction studies.^{9–11} The first complete X-ray crystal structure of a thiolatocobalamin was obtained for γ -glutamylcysteinylcobalamin,¹⁰ and in 2010 the high-resolution X-ray structure of GS-Cbl was finally obtained. In addition, the synthesis of thiolatocobalamins has been given considerable attention;^{10,12} however, only one investigation of the electrochemistry (cyclic voltammetry) of GS-Cbl has appeared in the literature.¹³

The high binding constant of GSH for aquocob(III)alamin at physiological pH has a number of chemical consequences,

Received: February 8, 2012

Revised: April 20, 2012

Published: May 8, 2012



including the fact that the redox potential for reduction of the Co^{3+} in cobalamin is moved about 0.9 V negative when ligated by glutathionyl, i.e., on going from $\text{H}_2\text{O}\text{-Cbl(III)}^+$ to GS-Cbl(III). This means that the Co^{2+} species, cob(II)alamin, will not form from GS-Cbl by NADPH reduction so that this reduced form of cobalamin would not be available to react with xenobiotic epoxides in mammalian metabolism.¹⁴ We showed that NO reacts directly with GS-Cbl(III)¹⁵ to give nitrosylcobalamin, which is the Co^{2+} reduced NO-Cbl(II) species. Also of importance is that NO reacts directly with Cbl(II) with a high binding constant ($\approx 10^9$) but does not react directly with $\text{H}_2\text{O}\text{-Cbl(III)}$.¹⁶ This fact led us to suggest that GS-Cbl(III) might protect biological systems against the effects of excess NO.¹⁵ On the other hand, it has been suggested that GS-Cbl might regulate NO production by nitric oxide synthase (NOS) by promoting all three isoforms of NOS and by inhibiting the iNOS and eNOS isoforms.¹⁷ Subsequently, it was found experimentally that various corrinoids can indeed inhibit NOS, and molecular modeling showed that it was possible for corrinoids to access the large heme and substrate binding pocket of NOS.¹⁸ Unfortunately, GS-Cbl was not tested in this study.

GS-Cbl may have an important role to play in human biology as an intermediate in the formation of the Me-Cbl coenzyme. In this role, it appears that GS-Cbl is more active than other forms of cobalamin in promoting MetH activity.^{3a} The mechanistic details of this enzymatic reaction involves direct methyl transfer from the Me-Cbl cofactor to homocysteine (Hcy) producing methionine and cob(I)alamin, which is recycled to Me-Cbl(III). In fact, there is a complicated metabolic web involving various forms of cobalamin, GSH, and GS-Cbl, since the transsulfuration pathway takes Hcy \rightarrow cystathione \rightarrow cysteine \rightarrow GSH. Thus this source of GSH can react enzymatically with $\text{H}_2\text{O}\text{-Cbl(III)}$ to make GS-Cbl, which then can promote MetH enzyme activity.

An additional biological role for GS-Cbl is as an agent that can modulate oxidative stress. Elevated levels of Hcy and low serum levels of vitamin B₁₂ and folate are associated with cardiovascular disease and neurological dysfunction such as found in patients with Alzheimer's disease,¹⁹ which is also associated with oxidative stress.²⁰ In fact, it was recently found that pretreatment of Sk-Hep-1 cells with GS-Cbl or N-acetyl-L-cysteinyl-Cbl have antioxidant effects protecting the cells from the "pro-oxidants" Hcy and H_2O_2 .²¹ Furthermore, impaired MetH activity in the brain has been suggested to be associated with Alzheimer's disease,²⁰ and for this reason, it was suggested that GS-Cbl may have value in treating neurological disease because it would be a substrate for the eventual biosynthesis of Me-Cbl.²⁰

In view of its biological significance, we are concerned here with the electronic and geometric structure of GS-Cbl, its optical spectroscopy, and the chemical nature of its Co(III)-S bond in comparison with other axial ligand bonds to Co(III) in cobalamins. We examine this structure with density functional theory (DFT) calculations of truncated models of the entire molecule. Furthermore, we compare the electronic spectroscopy (ultraviolet-visible (UV-vis) and circular dichroism (CD)) of GS-Cbl(III) with time-dependent DFT (TD-DFT) calculated spectra. Activation of $\text{Co}^{3+}-\text{C}$ or $\text{Co}^{3+}-\text{S}$ bond breaking is an important property of the enzyme mechanisms involving Me-Cbl, Ado-Cbl, and GS-Cbl. The nature of this Co-ligand bond is especially germane if GS-Cbl is involved in the enzymatic biosynthesis of Me-Cbl and Ado-Cbl. Very recently,

a comparison of the Co-S and Co-C bonding in GS-Cbl and Me-Cbl by spectroscopic and computational methods with B3LYP was reported by Conrad and Brunold.²² Herein we examine additional aspects in characterizing this bonding and in the simulation of the electronic spectroscopy by comparing both B3LYP and BP86 density functionals and using vacuum and water-solvent models.

The general structure of an R-axial-substituted hexacoordinated cobalamin is shown in Figure 1. In cobalamins,

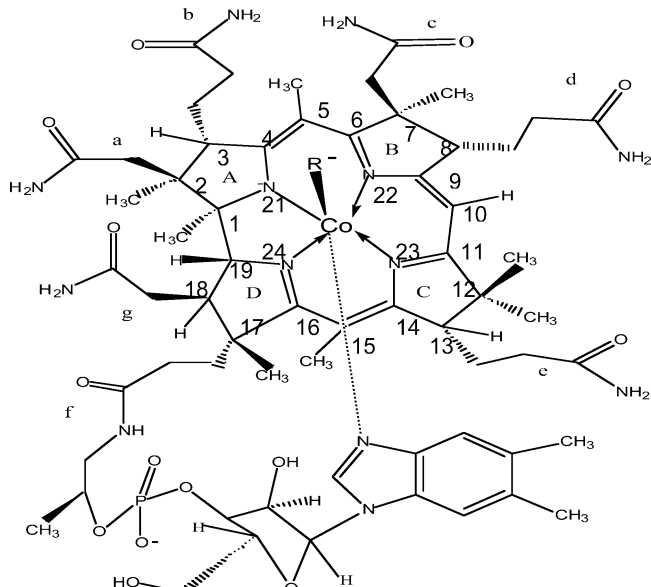
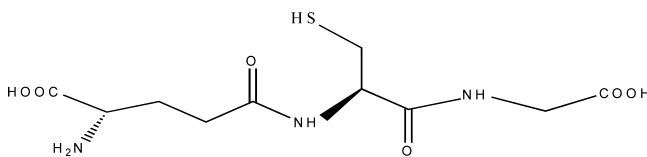


Figure 1. Molecular structure of neutral R-Co(III)balamins with rings A–D and side chains a–g.

the Co ion is equatorially coordinated by four pyrrole nitrogens from the macrocycle corrin ring. This ring contains four pyrrole groups (A–D) with a negative charge residing in the corrin ring and with seven labeled side-chains on the ring. There are several methyl groups on the ring, and six of the labeled side-chains (a–e, g) are ethyl or propyl amides. A seventh side-chain (f) contains a nucleotide with a negatively charged phosphate group, a ribose, and the 5,6-dimethylbenzimidazole (DBz) coordinating base, which acts as a lower axial ligand. For Co^{3+} cobalamins, the upper R-axial ligand can be either noncharged as with a H_2O ligand, giving an overall +1 charge in aquoco(III)balamin, $\text{H}_2\text{O}\text{Cbl}^+$, or negatively charged as in CH_3^- or GS^- , giving an overall neutral molecule as in methylco(III)balamin (Me-Cbl) and GS-Cbl(III). The R group above the plane of the corrin ring is said to be in the β -axial position, and the DBz base below the plane is said to bind in the α -axial position. In most of the truncated model compounds used for electronic structure calculations, the side-chains are replaced by hydrogen, including the f side-chain, so that there is only one full negative charge coming from the corrin ring. Then the models of Me-Cbl(III) and GS-Cbl(III) have a charge of +1, but the model for $\text{H}_2\text{O}\text{-Cbl(III)}^+$ has +2 charge.

The glutathionyl ligand, GS^- , is formed when a proton is lost from the sulfur atom of GSH.

The UV-vis absorption spectrum of cobalamins has been used to differentiate between various types of cobalamins. The organo-metallic Me-Cbl and Ado-Cbl and other carbanion-cobalamins were designated in a group called "anomalous" or



"atypical" compared with the H₂O-Cbl⁺ and CN-Cbl, which represent the "normal" or "typical" group.^{23–25} Five bands were originally singled out^{23,24} as manifested in the H₂O-Cbl⁺ spectrum (red curve, Figure 2A), two prominent bands in the

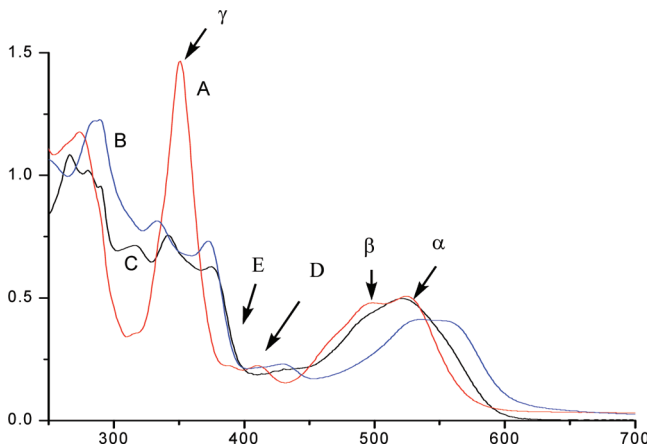


Figure 2. UV-vis spectra of R-cobalamins: (A) aquo-Cbl(III), (B) GS-Cbl(III), (C) methyl-Cbl(III), all at pH 5.

500–600 nm region called α (long wavelength) and β (short wavelength), two low intensity bands around 400 nm called the D (long wavelength) and E (short wavelength), and the intense γ band around 350 nm. These band positions are quite sensitive to the β -axial ligand and the solvent.^{23,24} The so-called atypical cobalamins have the γ band shifted to longer wavelength (Figure 2B,C). An interesting question is how to explain the spectral differences. It was pointed out some time ago⁸ that the spectrum of GS-Cbl (purple, Figure 2B) was very similar in position and shape to that of Me-Cbl (black, Figure 2B) in the γ -band region.

The shift of the γ -band in cobalamins is related to the σ -donor strength of the β -axial ligands,²⁴ and this has been explicitly shown experimentally for Co–S bonded cobalamins.⁸ A large number of common β -axial ligands give cobalamins in the typical group such as H₂O, CN⁻, OCN⁻, NH₃, Br⁻, Cl⁻, OH⁻, NO₂⁻, N₃⁻, pyridine, and CH₃CO₂⁻,^{23,24} however, there are also a large number of β -axial ligand giving cobalamins in the so-called atypical group including the cobalamins: Me-Cbl, Ado-Cbl, CH₂=CH-Cbl, S₂O₃²⁻-Cbl, Cysteinyl-Cbl, as-well-as GS-Cbl.^{24,26} In the later group, the ligand not only shifts the γ -band to longer wavelength, but causes the band to split into at least two bands on either side of the γ -band and shifts the α/β region to the red. The similar shift in the α/β region in GS-Cbl and Me-Cbl has also been pointed out by Conrad and Brunold.²² Brunold and co-workers concluded that there is an increase in the density of molecular orbitals (MOs) near the highest occupied MO to the lowest unoccupied MO (HOMO–LUMO) gap and extensive mixing between Co 3d and corrin π orbitals for the atypical Me-Cbl and Ado-Cbl compounds, which explains the shift in the spectra.²⁷ It is also seen in Figure 2 that the α/β region in GS-Cbl is shifted farther to the red than in Me-Cbl, and a similar shift is observed in

cysteinyl-Cbl.²⁶ This shift is evidently related to the thiolato ligand. Thus, the features of the thiolato-Cbl spectra will strongly depend on the Co(III)-S ligand bond and how this coordination communicates with the corrin ring. In fact, the M–S_{thiolate}²⁸ bond can be quite covalent and involve both a σ and π nature.

An interesting question related to cobalamin electronic spectra is whether there is a vibronic progression in the α/β region of the UV–vis spectrum. Firth et al.²³ suggested that this occurred for Me-Cbl, and this suggestion was repeated in Pratt's review chapter.²⁵ However, in a more detailed consideration made by comparing deconvoluted experimental UV–vis peaks with DFT calculated electronic transitions, it was concluded that a vibrational progression of the long axis excited state corrin ring vibration (ca. 1250 cm⁻¹) occurs in H₂O-Cbl⁺ but not in Me-Cbl since the deconvoluted peaks show different energy splittings in this region for the latter.²⁷ We will further consider this question for GS-Cbl. Of considerable interest is the solvent effect in the DFT spectral simulations, and also whether the transitions suggested to be vibronic can in fact be pure electronic transitions.

There have been a large number of electronic structure calculations for cobalamins. Very early studies of the UV–vis electronic spectra were made using the semiempirical Hückel and Pariser–Parr–Pople methods.^{39–31} More recently, many investigations have been made with DFT and TD-DFT, however, mostly for molecules with the Co–C bond. DFT calculations were used for structure optimization of various alkylcobalamin models and for analyzing the bond distances connected with their bond dissociation enthalpies (BDEs)^{32,33} for effects that might influence the Co–axial ligand bonding,^{34,35} for trans-axial ligand effects on the Co–C bond,³⁶ and for the influence of electric field on the Co–C bond.^{33,37} Other DFT calculations were made for a coenzyme protein bound model,³⁸ the vibrational frequency analysis of Me-Cbl³⁹ and Ado-Cbl,⁴⁰ and the electronic properties of the reduced forms of the cobalamin molecule.^{41–45,36b,44,45} It has also been concluded by theoretical means^{37,36} that the lower axial N-base does not have a large effect on Co–C bond distance of the upper axial ligand. A MO model that explains this anomalous effect was proposed in a study that used molecular dynamics within the Carr–Parrinello approach and the Becke–Perdew DFT-LSD theory.⁴⁶ Recently Jensen and Ryde⁴⁷ have reviewed electronic structure calculations of protein and nonprotein cobalamin systems. They point out that hybrid functionals such as B3LYP are less suitable than nonhybrid functions such as BP86 for studies of organometallic systems involving energy considerations, while both functionals perform well for geometric structure calculations. Similar considerations were explored in a comparison of three different functionals, B3LYP, BP86, and revPBE, for the strengths of the Co–C bond in several model cobalamins, where it was shown that B3LYP underestimates the bond strength, while BP86 is closer to experimental values.⁴⁸ Also, a comprehensive study of R-Co and Co–N_{ax} bond lengths for 28 corrin containing models was made at the BP86/6-31(d) level and showed good reliability with respect to experiment.⁴⁹

The nature of the axial Co–S and Co–C bond with respect to the Co–N_{ax} bond has been considered with DFT calculations, EXAFS measurements, and crystal structures.⁵⁰ Here DFT calculations of bond distances in truncated models of SO₃Cbl and (NH₂)₂CSCbl were compared with X-ray crystal structures. Starting from highly resolved crystal structures, the

electronic structures of MeCbl,⁵¹ CNCbl,⁵² and AdoCbl⁵³ have been calculated by the orthogonalized linear combination of atomic orbitals (OLCAO) DFT method. These were single-point calculations but used the entire R-Cbl without truncation. On the other hand, excitation calculations to obtain the electronic transitions were not performed. Most of the above electronic structure calculations of cobalamins have been made for the vacuum state.

Characterization by TD-DFT calculations of the nature of the excited states and of the excited state transitions for cobalamins have also been of much interest since the UV-vis and electronic CD (ECD) spectra show so many features of cobalamins that depend on the type of axial ligands, the oxidation state and coordination number of Co, and the solvent and enzyme environment. The semiempirical calculations of Day,²⁹ based on a 13 atom, 14 π electron, conjugated equatorial ligand model of the corrin ring, show that the α and γ bands shift to lower energy with the donor power of the axial ligands in agreement with experiment. The first extensive TD-DFT excited state study and simulated UV-vis spectra were calculated by Kozlowski and co-workers with the popular Becke three-parameter hybrid exchange functional with the Lee-Yang-Parr correlation functional (B3LYP) for truncated cobalamin models designated CN-Co(III)-corrin-CN and CN-Co(III)-corrin-Imidazole.⁵⁴ The TD-DFT calculations show a shift of HOMO \rightarrow LUMO transition to higher energy when $-CN$ is replaced by imidazole. This mirrors the α band experimental results on going from CN-Cbl-CN to CN-Cbl in the UV-vis spectra. An excited state calculation has been made for Co(I)-corrin with both an all-electron and an effective core potential (ECP) basis set.⁴³ The assignments for the higher energy states were found to be better with the all-electron calculation than with the ECP calculation.

A number of very detailed excited state studies and comparisons with experimental results have been made by Brunold and co-workers. The previously discussed investigation²⁷ for models of $H_2O\text{-Cbl(III)}^+$, Me-Cbl(III), CN-Cbl(III), and Ado-Cbl(III) was made with DFT optimizations of truncated models based on crystal structures. This work again showed that TD-DFT could predict the shifts with change in the upper axial ligand in the α and γ bands. TD-DFT simulated absorption spectra of Me-Cbl have also been calculated as a function of different axial ligand bond lengths (Co-C and Co-N_{ax}) and corrin ring distortions in order to simulate spectral effects of the enzyme (MMCA) interaction with the cofactor.⁵⁵ Electron density difference maps (EDDMs) were calculated in the former case⁵⁵ to examine the nature of the major absorption bands. These show for the α band that electron density is removed from the Co-C bond in addition to the $\pi \rightarrow \pi^*$ corrin ring-based transition, while the D/E and γ bands are characterized as a metal-to-ligand charge-transfer (MLCT) excitations.⁵⁵

Recently TD-DFT was used to simulated electronic absorption spectra of Me-Cbl(III),⁵⁶ CN-Cbl(III) and Me-Cbl(III),⁵⁷ and Me-Cbl(III) and ethyl-Cbl(III)⁵⁸ truncated models. In the first study, either imidazole or water was used in the truncated structure, and the hybrid B3LYP exchange correlation functional was compared with the B86 gradient corrected functional with a 6-31G(d) basis set for all atoms, except Co, where a VTZ basis set was employed. TD-DFT overestimates the excited state energies, and usually a simple shift of all lines in the simulated spectra is used for comparison to experimental results. However, in this study, a two-parameter

fit was used to improve the scaling of the calculated to the experimental spectrum of MeCbl(III) at pH 7. It was found that B3LYP is better at describing corrin $\pi \rightarrow \pi^*$ excitations, while B86 did a better job at describing metal-to-ligand excitations. It was also found that in the α/β band region, the BP86 calculation gives three transitions, whereas in B3LYP, only one intense transition is found.⁵⁶ Also, BP86 TD-DFT calculations in CNCbl show that using a solvent environment improves simulation of spectral features. It also shows that the origin cannot be attributed to a single transition but that there are multiple electronic transitions near the origin.⁵⁷ In a follow-up study,⁵⁸ both singlet and triplet excited states were calculated at the BP86/6-31G(d) level as a function of the Co-C bond distance. Electron density difference plots show that in the S₀-to-S₁ transition, charge density flows from both the Co ion and from the axial σ bond region to the corrin ring. This is somewhat similar but not exactly the same as that found with a B3LYP EDDM, where the α/β band transition is described as electron density loss from the Co-C bond region and alternating gain and loss from the conjugated portion of the corrin ring.⁵⁵

In the present work, we characterize the geometry and electronic structure of various GS-Cbl models by all-electron DFT and TD-DFT studies of the full glutathionyl ligand in the β -axial position of a cobalamin model. In the very recent study of GS-Cbl by Conrad and Brunold,²² only the first atom of this ligand was included in the QM part of the model calculation. Also, we examine the effect of the lower axial base, the density functional (B3LYP or BP86), and the effect of a water solvent model on geometric optimizations and the simulation of electronic spectra of GS-Cbl. Thus DFT and TD-DFT calculations were made in vacuum and with a conductor polarized continuum model (cpcm) water solvent model with both B3LYP and BP86 methods with the 6-311G(d,p) basis set. We found the two density functionals and vacuum versus water solvation model did not have much of an effect on DFT geometric optimized structure, but they have substantial effect on the bonding energies, the nature of the MOs, and the optical spectra simulations. Furthermore, there is a quantitative improvement with the BP86 functional over the B3LYP hybrid exchange correlation functional in the estimation of homolytic dissociation energies of Me-Cbl and GS-Cbl, and in simulating excited state transitions in the electronic spectra of GS-Cbl.

II. EXPERIMENTAL AND COMPUTATIONAL METHODOLOGY

Aquocobalamin(hydroxy-cobalamin-HCl) and GSH were obtained from Sigma-Aldrich Chemical Co. in <97% purity. UV-vis spectra were run with an Aligent model 8453 spectrometer, and CD spectra were run with a Jasco J-810 spectrometer at ambient temperatures. GS-Cbl was made up in solution by adding a slight excess of GSH to aquocobalamin (\approx 1:1 molar ratio). The GS-Cbl UV-vis spectra for these solutions were identical to solutions made from solid authentic GS-Cbl kindly supplied by Nicola Brasch. Deionized-distilled water was used to make up all solutions and all chemicals, including those to make up buffers, and salt solutions were analytical reagent grade.

A full geometry optimization was made for the ground state (DFT) followed by calculation of the excited state (TD-DFT) transitions. All calculations were made using the Gaussian 03 (G03)⁵⁹ or Gaussian 09 (G09)⁶⁰ package of programs to the default convergence criteria of Gaussian code 1.00D-08 on a

root-mean-squared (rms) density matrix within 128 cycles, 1.00D-06 on MAX density matrix, and 1.00D-06 on energy. The cobalamin systems were calculated both in the gas phase and for a solvent (water) environment with the cpcm.⁶¹ Calculations with TD-DFT have been implemented in the Gaussian code based on the linear response theory⁶² and our TD-DFT calculations conformed to nonequilibrium vertical transitions. With G03 and G09, all calculations were made with the 6-31G(d,p) basis set⁶³ except for two NBO calculations made with 6-31G(d,p). For the GS-Cbl model, we compared the B3LYP^{64,65} hybrid exchange correlation functional with the BP86 functional, the Becke–Perdew^{66,67} XC-potential, with generalized gradient approximation (GGA), utilizing G09 with the above basis set.

The AOMIX program⁶⁸ was used to analyze MO compositions, partial density of states (DOS) between molecular fragments, generalized Wiberg and Mayer bond orders, charge decomposition analysis (CDA), and energy decomposition analysis (EDA). Natural bond order (NBO) analysis as implemented in G03 and G09 was made on gas phase and aqueous ground state structures, and excited state transitions were analyzed with the natural transition orbitals (NTOs) of Martin⁶⁹ as implemented in G09. NTO analysis gives hole and electron orbital representations (isosurfaces) for the electronic transition density matrix for a given excited state transition.

At least three types of excited state calculations were carried out for each of the cobalamin species. These consisted of a simple calculation (i) of optimized ground state and excited state transitions of the molecule without considering any solvent effects. Another type (ii) was done in which the molecule was optimized without taking into account any solvent effects, but the excited state calculations were done with a solvent model. Finally, type (iii) calculations were done where the solvent was taken into account at every level, from the optimization to the energy transitions. It turned out that type (ii) calculations were closer to type (iii) than type (i) in excited transitions energies, but type (iii) matched the deconvoluted peaks better. With the G03 code, the geometry optimized calculations with a water cpcm model would not completely converge; however, with G09, this convergence was no longer a problem, and finally we only needed to compare the vacuum type (i) calculations to the solvent optimized type (iii) calculations for simulating electronic spectra. Calculations of oscillator strengths were transformed into spectra using a homemade program that had the option of Lorentzian or Gaussian broadening.

We have made DFT electronic structure calculations for R-cobalamins with a truncated model that includes the full corrin ring, but with all side chain groups replaced by hydrogen atoms and with the DBz or imidazole as the lower axial base (B) ligand as shown in Figure 3. These models can be denoted R-Co(III)-corrin-Bz or R-Co(III)-corrin-Im; however, sometimes we use Cbl for corrin, but in fact all calculations were for the chemical model in Figure 3.

The geometry optimized ground state calculations with the water environment converged for H₂O-Cbl(III) and Me-Cbl(III) truncated models with G03; however, for GS-Cbl(III) models, they would not converge with G03, but convergence was achieved with G09. We have utilized only one calculation with solvent that did not completely converge with G03, since its structure was found to be an adequate match to X-ray data. This was for the GS-Co(III)-corrin-Im model in water, where

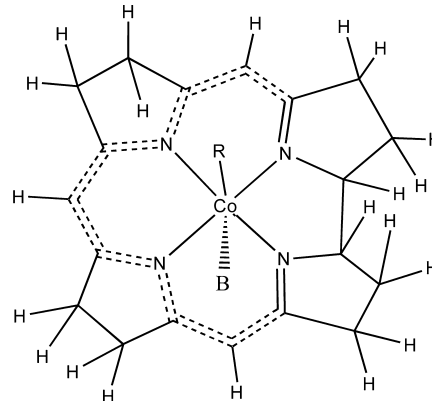


Figure 3. Truncated model for the axial-substituted cobalamins with all side chains replaced by hydrogen atoms. The 13-atom conjugated chain in the corrin ring is shown with dotted lines.

the geometry structure had converged for rms force, maximum displacement, and rms displacement but not for the maximum force, which was 0.001123 with a 0.00045 convergence criterion. A predicted change in energy (= -2.953641D-05) was found. All other calculations for all truncated models converged completely.

III. RESULTS AND DISCUSSION

A. Geometry of GS-Cbl(III) Models. We have optimized the geometry of six truncated models of GS-Cbl(III). These models are GS-Co(III)-corr-imidazole (GS-CblIm⁺) and GS-Co(III)-corr-dimethylbenzimidazole (GS-CblBz⁺) in the gas phase and in water solvent all at the B3LYP level, GS-CblBz⁺ in water solvent at the BP86 level, and a model where the GS-ligand of GS-CblBz is in the zwitterion form. In most calculations, the glutathionyl ligand was considered to have both carboxylate groups protonated with a single negative charge on the sulfur so that the calculation is for a singly positively charged cobalamin molecule. In the zwitterionic form, the ligand is now considered to have two negative charges since both carboxylate groups are ionized and the amine group on the glutamate moiety is protonated, and the sulfur is negative so the GS(zwitter)-Co(III)-corr-Bz is neutral. The zwitter ionic form is the major form of GSH in solution between pH 5–9.⁷⁰ We compare these optimized structures with the known high-resolution X-ray crystal structure of GS-Cbl.¹¹ We also optimized a model, Glu-Cys-Co(III)-corr-Bz (GluCysCblBz), with the γ -glutamylcysteinyl axial ligand for comparison with the X-ray structure of γ -glutamylcysteinylcob(III)alamin. Thus we have six optimized truncated chemical models of GS-Cbl that can be compared with its known X-ray structures and one optimized model of γ -GluCys-Cbl for comparison with its X-ray structure. Also, for GS-Cbl, a few bond distances are available from EXAFS data.⁸

Figure 4 shows a geometry optimized ball and stick structure of the GS-CblBz model in water solvent (cpcm). In this structure, as is true for all seven optimized structures, the four pyrrole N_{eq} equatorial atoms and the S_{ax} and N_{ax} axial ligand atoms form a slightly distorted octahedral structure with the central Co(III) ion. The truncated corrin macrocycle has C₂ symmetry along the short axis (SA) of the ring formed by the line from C10 and the bisector of the C1 and C19 bond. The long axis (LA) of the corrin ring is the distance between C5 and C15 and approximately bisects the two six-membered rings

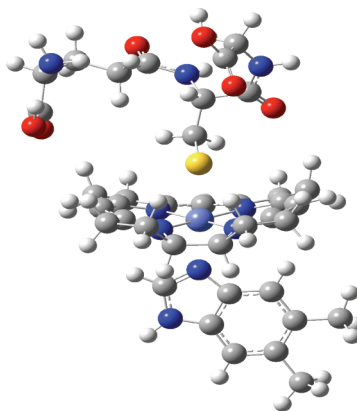


Figure 4. Optimized geometry of GS-Co(III)-corrin-Bz at the B3LYP/6-311G(d,p) level with the cpcm solvent model.

involving $\text{CoN}_{21}\text{C}_{4}\text{C}_{5}\text{S}_{6}\text{N}_{22}$ and $\text{CoN}_{24}\text{C}_{16}\text{C}_{15}\text{C}_{14}\text{N}_{23}$ (Figure 1), which are opposite each other. The imidazole ligand has been used in two of the geometry optimized structures because, for one thing, it requires less computational effort and is similar to dimethylbenzimidazole, but more importantly because in the two mammalian B_{12} dependent enzymes, a histidine (containing imidazole as a base) binds the Co ion in the α -position.^{71,72} This ligand comes from a protein residue and replaces the DBz in the active site with the nucleotide tail folded back into a pocket of the protein.

A comparison of selected bond distances, bond angles, and dihedral angles of the six optimized geometries of GS-Cbl and one of GluCys-Cbl were compared to the high-resolution X-ray structures of GS-Cbl¹¹ and GluCys-Cbl.¹⁰ This data is given in Table S1 of the Supporting Information. The optimized geometric structure for six truncated models of GS-Cbl was made by varying the chemical structure, (α -axial base), solvent model, and the two DFT functionals, B3LYP and BP86. All show similar geometry for the Co coordination sphere with the average RMSD of the bond distances for six models of 0.0215 Å with a standard deviation of 0.0032 Å and the average RMSD for the angles of 1.55° with a standard deviation of 0.20°, both with respect to the experimental high-resolution X-ray data.¹¹

First it can be pointed out that it is well-known from X-ray structures that the axial ligands do not have much of an effect on the bond distances and angles in the corrin ring for the substituted cobalamins.^{9,72} It has also been pointed out¹¹ that EXAFS data for GS-Cbl are not highly accurate when compared with the X-ray structure data. Both X-ray structures,^{10,11} however, show a Co–S bond length about 0.02 Å shorter than any of our theoretical RSCbl models. All our calculations in Table S1 show the well characterized longer bond distances for the six-membered rings over the five-membered rings.^{10,11,72} These distances are about 0.01 Å larger than the X-ray data in our calculations. Also the calculations show that the Co–S bond distance is on average 0.23 Å larger than the Co–N_{ax} distance, which is the same value as found in the GS-Cbl X-ray results (Table S1). The agreement between the calculations and the high-resolution X-ray structures is extraordinarily good. Comparing the average value of the standard deviation of the RMSDs between the six models (0.00317 Å) with the average value of standard deviation from the average deviation within the six models (0.0112 Å) in an analysis of variance strongly indicates that there is no significant statistical difference between these RMS deviations for the various models. This

indicates that the two different axial bases, solvent or vacuum environment, or DFT functionals do not significantly effect the optimized geometry. The good agreement with experiment seems then to be related to the good quality size of the basis set.

The angle data in Table S1 is mainly taken from the angles involving the Co ion and the equatorial N atoms in the corrin ring and the Co ion and the S and N coordinating atoms of the axial ligands. The $N_{eq}-\text{Co}-N_{eq}$, $N_{eq}-\text{Co}-N_{ax}$, $N_{eq}-\text{Co}-S_{ax}$ are again very close to X-ray data varying by less than 1–2° from the X-ray structure data. These show clearly the distorted octahedral structure. The angle between the Co and the first two thiolate ligand atoms, $C_{Me}-S-\text{Co}$, for all calculation models is somewhat less, (by 1–3°) than the 111.3(2)° of the X-ray data and shows the typical C–S–M angle of metal thiolates, which is in the range 100–120°.²⁸ The fact that the angle is greater than 90° indicates a pseudo σ bond where the electron density is shifted away from the M–S bond.²⁸ Because all the models have very similar geometry, we have used results from both the vacuum and water environment geometric optimization to examine the bonding and electronic structure of the GS-Cbl(III) molecule.

The final row in Table S1 is the fold angle φ defined as 180°–Ang(C15CoC5), which is the fold angle across the C5…C15 vector.⁵⁵ This is similar to the upward fold angle for the X-ray data for both γ -GluCys-Cbl and GS-Cbl, which is defined as the dihedral angle between two planes formed from atoms N21C4C5C6N22C9C10 and from atoms C10C11N23C14–C15C16N24.^{10,11} The average value of φ of 22.8° for the seven models is close to the value of 24.7° from the X-ray data for GS-Cbl, which is the largest fold found for 26 cobalamins.⁷² Out of 26 cobalamins, only NCS-Cbl (22.4°) and γ -GluCys-Cbl (24.2°) have experimental fold angles larger than 19° (Table 1, ref 72). Thus our calculations reproduce rather closely the large fold angle for thiolatocobalamins. Also the calculations show that the models with benzimidazole have a larger fold angle than those with imidazole. X-ray structures for cobalamins where benzimidazole was replaced with imidazole also show a smaller fold angle, which has been attributed to the smaller bulk of imidazole with respect to the benzimidazole.⁷²

B. Electronic Structure and MOs. Figure 5 is a stacked bar graph made with AOMIX,⁶⁸ which shows the orbital electron energy around the HOMO–LUMO gap as a function of the % fragment composition in each MO. These are based on a Mulliken population analysis of the GS-CblIm in a gas model calculated at the B3LYP/6-311G(d,p) level. The fragments are the Co ion, the S in the GS-ligand, the corrin ring, the imidazole (Im) ligand, and the rest of the structure, i.e., the rest of the GSH without the sulfur. A related partial and total DOS plot for the same fragments is shown in Figure S1 of the Supporting Information. The HOMO is at –7.401 eV, and the LUMO is at –4.626 eV, giving a HOMO–LUMO gap of 2.78 eV.

If the calculation is done on the other models with benzimidazole replacing imidazole and in water solvent, the HOMO is pushed up (destabilized) about 1.8 eV, and the LUMO pushed up by about 2.5 eV, giving a HOMO–LUMO gap of about 3.1 eV. The partial % fragments show that the HOMO is dominated by a S atomic orbital ($p\pi$) with small contributions from the Co and corrin ring fragments, whereas the LUMO is dominated by the corrin ring antibonding orbital. The HOMO-1 energy level has contributions from the corrin ring but contains the bonding orbital contribution from the S–

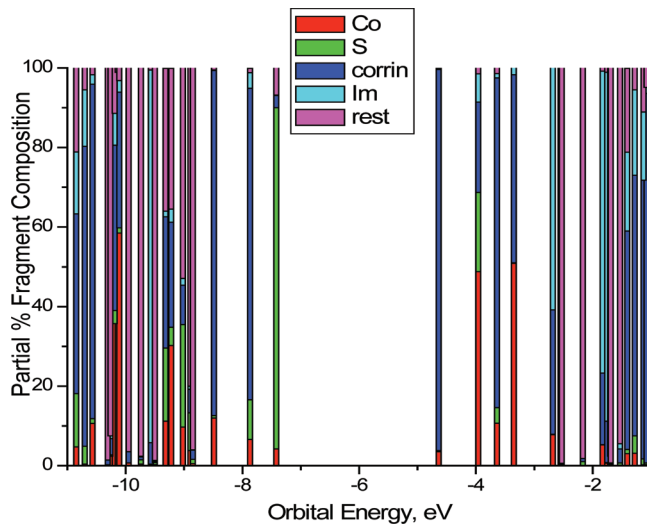


Figure 5. Orbital energies as a function of fragment for the GS-CblIm in gas model. Made with AOMIX-CDA for B3LYP/6-311G(d,p) SCF=Tight. The fragments are the Co ion, the S of the thiolate, the entire corrin ring with all side-chains replaced with H, the Imidazole (Im) ligand, and the rest of the molecule.

Co–N_{ax} structure. This is also seen in the isosurface of the orbital in Figure 6. Figure 6 is for the filled frontier orbitals near the HOMO, which show both bonding and antibonding interactions.

The isosurfaces are shown for the same frontier MOs from two different calculation models. The top MOs have Im as the base and were made in vacuum with B3LYP, and the bottom MOs have Bz as base and were made with BP86 and the cpcm water solvent model. In both cases, the HOMO shows a π antibonding interaction between the 3p_y sulfur orbital and the 3d_{yz} Co orbital and weak σ bonding between the Co and two N_{eq} groups in the corrin ring. On the other hand, the HOMO-1

shows the off-axis pseudo- σ bond formed between a sulfur 3p_z orbital and 3d_{z2} Co orbital. These MOs are very similar for the two models; however, the HOMO-2 is very different. Here the B3LYP GS-CblIm(gas) model shows no Co–S bond, whereas a π (Co(dyz)-Spy) bond is clearly evident in the GS-CblBzm (cpcm)BP86 model. With B3LYP, HOMO-2 for the GS-CblBzm in water is the same as the GS-CblIm vacuum model, so the difference in the HOMO-2 isosurfaces in Figure 6 is in the DFT exchange correlation potential and not the effect of solvent. Thus BP86 shows π bonding that is not seen with B3LYP.

Isosurfaces for all the MOs from MO 195 to MO 224, which are HOMO-19 to LUMO+9, are shown in the Supporting Information Figure S5 for the BP86 calculations. The excitation calculations with BP86 using NTOs (Figure S6) also demonstrate significant involvement of both σ bonded and π bonded Co–S in the molecule.

The bonding interactions can clearly be seen in the overlap population density of states (OPDOS) of AOMIX where the overlap population can be extended to user defined fragments such as the central metal atom, Co, the sulfur atom of the β -axial ligand, and the equatorial corrin ring ligand as in Figure 7. The positive overlap population, OP_{AB}, represents a bonding interaction, while negative values represent an antibonding interaction with OP_{AB,i} = $\sum_{a \in A} \sum_{b \in B} 2c_{ai}c_{bi}S_{ab}$. A,B are user defined fragments, and the sum for the ith MO is over the products of LCAO-MO coefficients, c_{ai} and c_{bi}, and the S_{ab} overlap integral. The negative going stick under the black Co–S line in Figure 7 at -7.40 eV is the π antibonding interaction in the HOMO, while the positive stick at -7.86 eV is the σ bonding interaction in the HOMO-1. There are several peaks in the OPDOS from the occupied MOs for Co–S bonding in the -12 eV to -7.4 eV region, while the strong bonding interactions between Co and the corrin ring are in the -14 eV to -11 eV region.

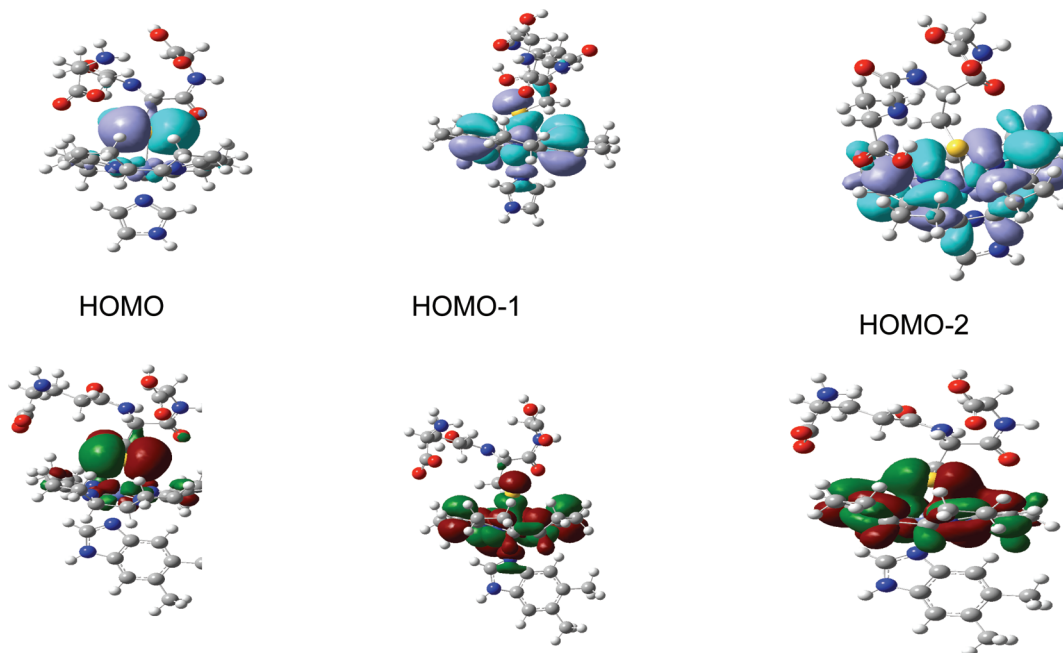


Figure 6. Frontier MO isosurfaces from the GS-CblIm (gas) B3LYP/6-311G(d,p) model on top and the GS-CblBzm (in H₂O)BP86/6-311G(d,p) model on the bottom. HOMO-1 shows the pseudo- σ Co–S bond, and HOMO-2 shows a π Co–S bond with BP86 but not with B3LYP.

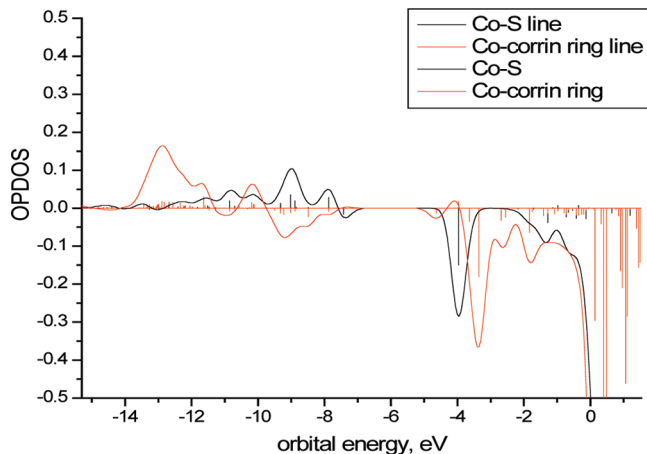
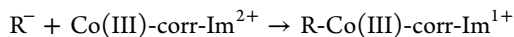


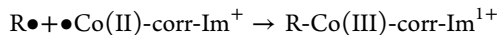
Figure 7. Overlap population (sticks) and OPDOS for Co–S and Co-corrin bonding in the GS-Cbl-Im gas-phase model (B3LYP/6-311G**) from AOMIX.

C. Binding Energies and Charge and Energy Decomposition Analysis (CDA and EDA)

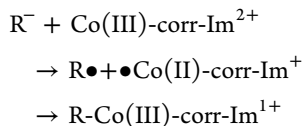
The binding energy for the model reaction



is the reverse of the heterolytic bond dissociation energy (BDE), where R^- is the anionic form of the β -axial ligand. The homolytic BDE is the reverse of the binding energy for the reaction



where $R\bullet$ is the radical form of the β -axial ligand, which binds to the reduced form of cobalamin. These two reactions are simply related by the reaction sequence



where the first step liberates redox energy when the anionic ligand donates an electron to the oxidized form of cobalamin. The second step is the coupling of the radicals, which bind to give $R\text{-Co(III)-corr-Im}^{1+}$. The binding energy can be calculated from the difference in energy between the optimized complex and the sum of each optimized reactant. In light of the recent study where the GS-Cbl model complex was compared with a MeCbl model at the B3LYP calculation level,²² it is interesting to compare our glutathionyl and methyl axial ligand complexes at the two DFT levels of calculation.

In Table 1 in columns 2 and 3, we compare the binding energies for the homolytic and heterolytic binding reactions for both B3LYP/6-311G(d,p) and BP86/6-311G(d,p) in vacuum when R is either glutathionyl or methyl. In terms of the BDE, it

is observed that the homolytic BDE is significantly larger for BP86 than B3LYP for both GS and Me radicals. The same correlation does not hold for the heterolytic BDE where the value for GS-Co(III)-corr-Im¹⁺ is less with BP86 than with B3LYP but about the same for the two functionals for Me-Co(III)-corr-Im¹⁺. Of course the effect of solvent should be included for accurate comparisons of the heterolytic BDE. The good value for the homolytic BDE result can be attributed to the calculation of the energy of the optimized radicals. In fact the experimental value of the homolytic BDE for Me-Cbl(III)^{73,74} was found to be 37 ± 3 kcal/mol, which is very close to the value 36.76 kcal/mol calculated by our BP86/6-311G(d,p) calculation, and much larger than the 23.51 kcal/mol calculated with our B3LYP method. Our results for this BDE in the Me-Cbl model with BP86 are slightly closer to experimental values than those found earlier with BP86 using the smaller 6-31G(d) (VTZ for Co) basis sets, where a homolytic BDE of around 41 kcal/mol was calculated.⁴⁸ With B3LYP our homolytic BDE is close to previously calculated values.⁷⁵

Further insight into the nature of the bonding interaction can be gained by using an EDA, as investigated by Kitaura and Morokuma,⁷⁶ and the related extended transition state (ETS) analysis of Ziegler and Rauk.⁷⁷ The binding energy of two fragments, A, B, in the complex, A–B, can be divided into the sum of a preparation energy, also called deformation energy, and the interaction energy: $E_{\text{binding}} = E_{\text{INT}} + E_{\text{prep}}$. Here the complex A–B stands for $R\text{-Co(III)-corr-Im}^{1+}$, the fragment A is the anionic form of R, and B is the Co(III)-corr-Im²⁺ complex. The preparation energy is the energy required to take fragments A and B from their ground state equilibrium geometry to their ground state geometry in the A–B complex. The interaction energy $E_{\text{INT}} = E_{\text{binding}} - E_{\text{prep}}$ can be directly calculated from the energy difference between the optimized A–B complex and the sum of the energy (single point calculations) of fragments A and B in their ground state geometry in the R-Cbl(III) complex. Table 1 shows the binding energy, the preparation energy, and the interaction energy for both GS[−] and Me[−] for the two functionals for the heterolytic case. Such a calculation for E_{INT} between the two fragments in the AOMIX analysis is without the basis set superposition error (BSSE) or zero point energy difference corrections. It is seen that the heterolytic binding energy with BP86 for the reaction with Me[−] (−250.97 kcal/mol) is substantially larger, about −90 kcal/mol, than for GS[−] (−161.66 kcal/mol). On the other hand, Table 1 shows that the preparation energy is around twice as large for GS[−] compared to Me[−]. Analysis of the individual preparation terms indicates that for the GS-Cbl model, about 66% of the preparation energy comes from the deformation of the Co-Corr-Im²⁺ fragment, while for the Me-Cbl model, 90% comes from this deformation.

Table 1. Binding Energy Analysis and EDA for Heterolytic and Homolytic Binding of R-Co(III)-corr-Im^{1+*}

DFT/6-311G(d,p)	R	$E_{\text{binding homo}}$	$E_{\text{binding hetero}}$	$E_{\text{interaction hetero}}$	$E_{\text{prep hetero}}$	$E_{\text{orbital hetero}}$	$E_{\text{steric hetero}}$	CT net e-donated
B3LYP	GS	−24.28	−166.02	−202.24	+36.22	−108.0	−94.24	0.72
BP86	GS	−29.77	−161.66	−203.67	+42.01	−119.4	−84.27	0.785
B3LYP	Me	−23.51	−246.61	−266.53	+19.92	−152.6	−113.93	0.761
BP86	Me	−36.76	−250.97	−268.75	+17.78	−165.8	−102.95	0.802

*Interaction energy is without the BSSE correction. All energies are in kcal/mol.

Table 2. CDA of the GS-Co(III)-Corr-Im⁺ with GS- and Me- as Fragment 2 and the Rest (Co-Corr-Im) of the Molecule as Fragment 1 for Major Contributions with a BP86/6-311G(d,p) Calculation^a

α -spin MO	donation $2 \rightarrow 1$		back donation $1 \rightarrow 2$		repulsion		residue Δ term	
	GS	Me	GS	Me	GS	Me	GS	Me
HOMO-8	0.001	0.000	-0.001	0.006	-0.002	-0.026	0.000	0.000
HOMO-7	0.000	0.005	0.000	0.004	0.000	0.006	0.000	0.000
HOMO-6	0.013	0.041	0.002	0.005	-0.008	0.000	0.001	0.000
HOMO-5	0.001	0.000	0.000	0.000	-0.001	0.000	0.000	0.000
HOMO-4	0.003	0.001	0.001	0.005	-0.001	-0.008	-0.001	0.000
HOMO-3	0.012	0.016	-0.001	0.001	-0.007	-0.024	-0.001	0.001
HOMO-2	0.001	0.002	0.000	0.007	-0.001	-0.008	0.000	0.000
HOMO-1	0.044	0.001	0.005	0.006	-0.063	-0.005	0.002	0.000
HOMO	0.010	0.041	0.004	0.005	-0.119	-0.057	0.000	0.000
sum over α -MOs	0.195	0.122	-0.003	0.036				
total $\alpha + \beta$	0.390	0.244	-0.005	0.073	-0.220 ^b	-0.147 ^b	-0.003 ^b	-0.002 ^b

^aAccording to the method of Dapprich and Frenking (ref 79) with both charge transfer and electronic polarization contributions. ^bTotal over OMOs.

The interaction energy between the two fragments can be partitioned between two energies: a steric energy and an orbital energy

$$E_{\text{INT}} = E_{\text{steric}} + E_{\text{ORB}}$$

which can be further partitioned into four terms. Thus the steric energy contains two terms, $E_{\text{steric}} = E_{\text{ES}} + E_{\text{EX}}$, where E_{ES} is the electrostatic interaction energy and E_{EX} is the Pauli repulsion and exchange energy. Likewise the orbital energy contains two terms: $E_{\text{ORB}} = E_{\text{CT}} + E_{\text{EP}}$, where E_{CT} is charge transfer donation energy and E_{EP} is electronic polarization energy that comes from the fragment-induced mixing of occupied and unoccupied orbital population. The orbital energy term gives a measure of the covalent stabilization due to all orbital interactions. Table 1 shows that the density functional does not dramatically affect the values of the interaction energy for both the GS-Cbl(III) and the Me-Cbl(III) models. However, the orbital energy is more negative with BP86 than with B3LYP, and the steric energy is less negative with BP86 for both model complexes. Since the R⁻ fragment has a -1 charge and the Co-Corrin-Im²⁺ has a 2+ charge, there is considerable electrostatic attraction that dominates the steric part of the interaction energy in both complexes. Considering the BP86 functional as the more reliable calculation, in this case, the orbital energy is 58.62% of the interaction energy for the GS-Cbl(III) model and 61.69% for the Me-Cbl model. Thus in both cases, more than half of the total interaction energy contains the bond stabilization due to charge donation and electronic polarization between the fragments. Table 1 shows the net charge transfer donation (CT) which is close to a full electron in both cases being 0.785 e⁻ for GS-Cbl(III) and 0.802 e⁻ for Me-Cbl(III) model as calculated with AOMIX. These calculations exclude electronic polarization effects in calculating the CT donation, and the analysis is called the extended charge decomposition analysis^{68,78} (ECDA).

The bonding can be further discussed in terms of donor–acceptor interactions using the CDA as calculated with the AOMIX program. The CDA is based on the model of Dewar–Chatt–Duncanson as formulated by Dapprich and Frenking.⁷⁹ In this method, the donation, back-donation, repulsion, and residue terms are calculated between fragments for each MO of the complex (Table 2). The wave function of the complex, R-Co-Corr-Im, is expressed in terms of a linear combination of fragment molecular orbital (FMO) of the ligand GS- or Me-

(fragment 2) and of the remaining fragment, Co-Corr-Im (fragment 1). Thus the donation (i) is from the mixing of the occupied fragment MOs (OMOs) of GS- (Me-) with the unoccupied fragment MOs (UMOs) of Co-Corr-Im, and the back-donation (ii) comes from the mixing of OMOs of Co-Corr-Im with the UMOs of GS- (Me-). On the other hand, the repulsion (iii) comes from the repulsive polarization of the OMOs of GS- (Me-) with the OMOs of Co-Corr-Im, and the residue term, Δ , (iv) comes from the mixing of the UMOs of GS-(Me-) with the UMOs of the Co-Corr-Im.⁸⁰ The sum of this latter Δ term is close to zero for both complexes (Table 2), which shows that both complexes can be classified as a donor–acceptor complex.⁸⁰

Table 2 also shows that the HOMO-1 has the largest amount of α -spin orbital charge donation for the GS-Cbl model, while the HOMO and HOMO-6 have the largest amount for the Me-Cbl model. In GS-Co(III)-corr-Im¹⁺, the donation is from the thiolate ligand fragment, RS-, to the rest of the complex, and, as seen from the isosurfaces, this is σ -charge donation from the S to the Co d orbitals. The total α -spin donation is 0.195 e, and that of the back-donation is -0.003 with a sum of total α -spin + β -spin donation, 2 → 1, of 0.390; however, the donation and the back-donation terms not only include charge transfer (CT) from occupied to unoccupied orbitals but also include electronic polarization changes in the orbitals. Thus the difference between the two terms is a measure of overall reorganization of the electron density and not the net CT. Thus it is difficult to separate the two effects in the small back-donation terms such as in the HOMO (0.004 e) and the HOMO-1 (0.005 e), which might indicate back-donation from Co to S or electronic polarization, Pl. These two MOs also show the largest repulsive polarization terms and make up most of the closed-shell repulsion. On the other hand, for the Me-Co(III)-corr-Im¹⁺ complex, there is considerable back-donation in seven of the nine MOs in Table 2 except for HOMO-3 and HOMO-5. Thus in the Me-Cbl model there is much more back-donation than in the GS-Cbl model.

The ECDA⁷⁸ isolates the charge donation from the electronic polarization. It shows a net 0.785 electrons transferred by charge donation from fragment 2 (RS-) to fragment 1 (Co-Corr-Im) with a net 13.9% electronic polarization between fragment 1 and fragment 2. In the Me-Cbl model case, the ECDA gives 0.802 electrons transferred with a net 19.7% electronic polarization between the fragments.

Examination of the change in the fragment orbital populations when binding in the molecule in terms of % FO contributions to OMOs and UMOs of the complex shows there is considerable electronic rearrangement. Most of the populations of the fragment orbitals do not change on going from separated fragments to bound fragments, i.e., OFO population from the separated fragments remain close to 100% occupied in the molecular complex and UFO remain close to 100% unoccupied in the complex. However, in GS-Co(III)-corr-Im¹⁺, there are dramatic changes for two of the fragment orbitals on forming the complex (BP86 calculation). These are the lowest unoccupied fragment orbital (LUFO) from fragment 1 (Co-Corr-Im) and the highest occupied fragment orbital (HOFO-1) from fragment 2 (GS-). In the complex, the LUFO of the Co-Corr-Im fragment is as expected no longer unoccupied and contributes 49.23% to OMOs, but 50.77% remains in UMOs in the GS-Co-corr-Im complex. These changes result from CT to this LUFO in the formation of the Co–S bond from the HOFO-1 of the GS⁻ fragment but also result from electronic polarization. On the other hand, while HOFO-1 of fragment 2 (GS-) still contributes 66.81% to OMOs in the complex, now 33.18% population has moved into UMOs of the GS-Co-Corr-Im. Some of these changes correspond to the electronic polarization, which would lower the amount of CT calculated by the CDA and shows the utility of the ECDA.⁶⁸ The situation is similar for the Me-Co-corr-Im complex, but CT donation comes from the HOFO not the HOFO-1. Here the LUMO on the Co-Corr-Im fragment contributes 60.73% to the OMOs and 39.27% to UMOs. Now it is the HOFO of the methyl anion that contributes 57.51% to OMOs and 42.50% to UMOs. Thus CT donation from ligand takes place, but again electronic polarization is still evident.

It is interesting to compare the two-center bond orders for different R in the R-Co-corr-Im model as calculated from the DFT in the gas phase. With AOMIX,⁶⁸ the generalized Wiberg and Mayer bond orders calculated from the canonical MOs in the nonorthogonal AO basis are the same for closed shell spin-singlet state calculation. The generalized two-center Mayer (Wiberg) bond order indices, B_{AB} , between fragments A and B are defined as

$$B_{AB} = 2 \sum_{a \in A} \sum_{b \in B} (PS)_{ab} (PS)_{ba} \quad (1)$$

where P is the total density matrix and S is the atomic orbital overlap matrix.⁸¹ A four fragment bond index calculation can be made with the axial ligand R, Co³⁺, the corrin ring, and the axial base as the four fragments. The generalized Mayer (Wiberg) bond orders between the β -axial ligand R and Co³⁺, with R = Me⁻, GS⁻, and H₂O, are 0.901, 0.778, and 0.257, respectively, in the R-Co-Corr-Im model complex with B3LYP/6-311G-(d,p). If the bond order comes primarily from the β -axial ligand atom attached to Co, then the Me-Co bond order is closest to a pure covalent σ organo-metallic bond. However, the above bond orders are between R and Co and so include interactions of other atoms in R with the Co ion, which could be attractive or repulsive, especially for the GS ligand. However, since the GS-Co bond order is very close to that of Me-Co, it does show a significant amount of covalent character especially in comparison to the quite low generalized Mayer (Wiberg) bond order for the O–Co bond from water. For comparison, the Wiberg bond index for Co–S in the orthogonal natural atomic orbital (NAO) basis for the GS-Co-corr-Im model is 0.682 (Table 4).

If a two fragment calculation is made with R and Co(III)-Corr-Im²⁺ as the fragments, then the bond indexes between the two fragments are 1.02, 1.03, and 0.342 for R = Me-, GS-, and H₂O, respectively, with B3LYP/6-311G(d,p) and 1.08 and 1.15 for R = Me-, GS-, respectively, with BP86/6-311G(d,p). In the case of GS-Co-corr-Im⁺, the higher bond index comes from interactions in addition to the S–Co bond. Thus, the four fragment calculation shows that there is a direct interaction of the GS⁻ ligand with the corrin ring fragment itself since this bond index is 0.180. On the other hand, the bond index for Me⁻ with the corrin ring is only 0.054, showing that the C–Co bond is indeed closer to a pure σ covalent bond than the S–Co bond. However, the EDA and CT donation results (EEDA) of Table 1 show the very similar nature of the electrostatic and orbital bonding interactions in the GS-Cbl and Me-Cbl models, although the homolytic and heterolytic BDEs of Me-Cbl are much larger than for GS-Cbl, and the detailed nature of the bonding MOs are quite distinct in the two complexes.

D. NBO Analysis of GS-Cbl Models. The NBO analysis⁸² was made for two molecular structures, GS-Co(III)-corr-Im and GS-Co(III)-corr-Bz, with the B3LYP and BP86 calculation models. We examined the NBO analysis for the effect of solvent, for changing the axial base, the basis set, and the density functional. Models A through D in Table 3 were made with the B3LYP hybrid density functional, while models E and F were made with BP86. Only model A had imidazole, the rest

Table 3. Natural Electronic Configuration for the Co Ion in Model Calculations and Hybrid Natural Bond Orbitals for Co–N_{eq} and Co–S_{ax}

(A) GS-Co(III)-corr-Im ⁺ B3LYP/6-311G(d,p), vac	Co[core]4s(0.29) 3d(7.47)4p(0.02) 5s(0.01)	$\sigma = 0.40(\text{sd}^{1.95})_{\text{Co}} + 0.92(\text{sp}^{3.27})_{\text{N}23}$ $\sigma = 0.40(\text{sd}^{1.94})_{\text{Co}} + 0.92(\text{sp}^{3.30})_{\text{N}24}$ $\sigma = 0.56\text{sd}^{2.26})_{\text{Co}} + 0.83(\text{s}^{0.05}\text{p}^{0.95})_{\text{S}ax}$
(B) GS-Co(III)-corr-Bz ⁺ B3LYP/6-311G(d,p), vac	Co[core]4s(0.33) 3d(7.25)4p(0.57)	$\sigma = 0.37(\text{sp}^{3.36}\text{d}^{2.24})_{\text{Co}} + 0.93(\text{sp}^{2.43})_{\text{N}21}$ $\sigma = 0.39(\text{sp}^{3.18}\text{d}^{2.26})_{\text{Co}} + 0.92(\text{sp}^{3.52})_{\text{N}23}$ $\sigma = 0.38(\text{sp}^{3.29}\text{d}^{2.27})_{\text{Co}} + 0.93(\text{sp}^{2.44})_{\text{N}24}$ $\sigma = 0.37(\text{sp}^{3.19}\text{d}^{2.21})_{\text{Co}} + 0.93(\text{sp}^{2.43})_{\text{N}22}$ $\sigma = 0.55(\text{sp}^{0.41}\text{d}^{1.76})_{\text{Co}} + 0.83(\text{s}^{0.11}\text{p}^{0.88})_{\text{S}ax}$
(C) GS-Co(III)-corr-Bz ⁺ B3LYP/6-311G(d,p), cpcm	Co[core]4s(0.33) 3d(7.24)4p(0.58)	$\sigma = 0.39(\text{sp}^{3.33}\text{d}^{2.40})_{\text{Co}} + 0.92(\text{sp}^{2.48})_{\text{N}21}$ $\sigma = 0.37(\text{sp}^{3.31}\text{d}^{2.26})_{\text{Co}} + 0.93(\text{sp}^{2.45})_{\text{N}23}$ $\sigma = 0.39(\text{sp}^{3.29}\text{d}^{2.27})_{\text{Co}} + 0.92(\text{sp}^{2.44})_{\text{N}24}$ $\sigma = 0.37(\text{sp}^{3.41}\text{d}^{2.34})_{\text{Co}} + 0.93(\text{sp}^{2.44})_{\text{N}22}$ $\sigma = 0.53(\text{sp}^{0.47}\text{d}^{1.70})_{\text{Co}} + 0.85(\text{s}^{0.12}\text{p}^{0.87})_{\text{S}ax}$
(D) GS-Co(III)-corr-Bz ⁺ B3LYP/6-311G(d,p), cpcm	Co[core]4s(0.28) 3d(7.45)5s(0.01)	$\sigma = 0.40(\text{sd}^{1.94})_{\text{Co}} + 0.92(\text{sp}^{3.34})_{\text{N}23}$ $\sigma = 0.40(\text{sd}^{1.94})_{\text{Co}} + 0.92(\text{sp}^{3.34})_{\text{N}24}$ $\sigma = 0.52(\text{sd}^{2.17})_{\text{Co}} + 0.85(\text{s}^{0.05}\text{p}^{0.95})_{\text{S}ax}$
(E) GS-Co(III)-corr-Bz ⁺ BP 86/6-311G(d,p), vac	Co[core]4s(0.29) 3d(7.56)5s(0.01)	$\sigma = 0.62(\text{s}^{0.05}\text{d}^{0.94})_{\text{Co}} + 0.79(\text{s}^{0.04}\text{p}^{0.96})_{\text{S}ax}$
(F) GS-Co(III)-corr-Bz ⁺ BP 86/6-311G(d,p), cpcm	Co[core]4s(0.29) 3d(7.56)5s(0.01)	$\sigma = 0.60(\text{s}^{0.06}\text{d}^{0.94})_{\text{Co}} + 0.80(\text{s}^{0.05}\text{p}^{0.95})_{\text{S}ax}$

had the DBz base, Bz. Most models were optimized with the basis set 6-31G(d,p); however, for two models B and C, the smaller 6-31G(d,p) basis set was used, which was found to effect the NBO analysis. In all, six models were taken for NBO analysis. Table 3 shows the natural electronic configuration for Co and the σ natural bond orbitals found by the NBO analysis for these models. It is seen that the same three σ bond orbitals are found in models A and D, the same five σ bond orbitals are found in models B and C, and the same single σ bond orbital is found in models E and F.

The hybrid natural bond orbital analysis found for these models follows the bonding picture stressed by Weinhold and Landis.⁸³ Symmetry considerations allow us to predict the atomic orbitals that will be involved in the hybrid orbitals. Tetragonal distortion of a six-coordinate geometry reduces symmetry O_h to C_{4v} .⁸⁴ The local symmetry for GS-Cbl around the central Co is C_{4v} . This means that the six σ bonds have a reducible representation, which may be resolved as $\Gamma_\sigma = 3A_1 + B_1 + E$. Thus the hybrid bonding orbitals can only involve combinations of possible NAO from the set $A_1(s, p_z, d_{z^2})$, $B_1(d_{x^2-y^2})$, and $E(p_x, p_y$ and $d_{xz}, d_{yz})$. Here d_{xy} which has B_2 symmetry, is a nonbonding orbital. In model A, the sd^2 natural hybrid orbital (NHO) on the Co should involve the $4s$, $3d_{z^2}$, and $3d_{x^2-y^2}$ orbitals. In models B and C, the sp^3d^2 NHO on the Co should involve the $4s$, $4p_x$, $4p_y$, $4p_z$, $3d_{z^2}$, and $3d_{x^2-y^2}$ orbitals. The NHO on the ligand N atoms binding to Co are sp^2 or sp^3 , and the NHO in the ligand S_{ax} σ bond is almost pure p_z . These NHOs should come from A_1 and E symmetry orbitals. Models E and F show almost a pure $3d_{z^2}$ orbital on Co bonding to $3p_z$ on S_{ax}. In every NBO model in Table 3, there is 1.8 to 1.9 occupation of the three lone pairs on Co. The three Co lone pairs should come from the $3d_{xy}$, $3d_{xz}$, and $3d_{yz}$ Co atomic orbitals. The antibonding non-Lewis orbitals of the latter could enter into π bonding with one of the S_{ax} lone pairs.

The polarization coefficients for all the Co–N_{eq} natural localized hybrid bond orbitals in Table 3 in models A, B, and C are very similar, being around 0.39 for the Co hybrid and around 0.92 for the N_{eq} hybrid. With $100|c_A|^2$ being the percentage of the NBO on each hybrid, this gives around 15% on the Co NHO and 85% on the N_{eq} NHO. Thus most of the population is on the equatorial nitrogens, indicating coordinate covalent bonding with the bond heavily polarized toward the pyrrole nitrogen. Although all the models show somewhat different NHO on Co for the Co–S bond, all of the polarization coefficients are very similar. Thus for the Co–S_{ax} bond, the polarization coefficients give around 29% on the NHO of the Co and around 71% on the NHO of the S_{ax}. Because of the CT from the sulfur, this bond is less polarized than the Co–N bonds.

The localized NBO analysis of the Wiberg bond index in the natural atomic orbital (NAO) basis (Table 4) illustrates that the bond indices in models A (B3LYP in vac), D (B3LYP with cpcm) and F (BP86 with cpcm) all at the larger 3- ζ basis set 6-311G(d,p) are more similar than for model C (B3LYP/6-31G(d,p) with cpcm) with the smaller basis set. The Wiberg bond indices, W_{AB} , in the NBO output come from the density matrix in the NAO basis. Here W_{AB} is the sum of the squares of the off-diagonal density matrix elements between atoms⁸⁵

$$W_{AB} = \sum_{a \in A} \sum_{b \in B} (P_{ba})^2 = 2P_{jj} - P_{jj}^2 \quad (2)$$

which is equal to twice the charge density in the atomic orbitals P_{jj} minus the square of the charge density. The Wiberg bond

Table 4. Wiberg Bond Index in NAO Basis

bond	(A) GS-Co(III)-corr-Im ⁺ B3LYP/6-311G(d,p), vac	GS-Co(III)-corr-Bz ⁺ B3LYP, cpcm			(F) GS-Co(III)-corr-Bz ⁺ BP86/6-311G(d,p), cpcm
		(C) 6-31G**	(D) 6-311G**		
Co–N ₂₃	0.347	0.478	0.349	0.377	
Co–N ₂₁	0.390	0.514	0.387	0.424	
Co–N ₂₄	0.386	0.514	0.388	0.424	
Co–N ₂₂	0.351	0.478	0.346	0.375	
Co–N _{ax}	0.202	0.378	0.239	0.250	
Co–S _{ax}	0.682	0.874	0.619	0.634	

index in the orthogonal NAO basis does not contain the overlap integral that is in the Mayer bond index, B_{AB} , in equation 1. Model A calculated in vacuum with imidazole shows a lower bond index for the Co–N_{ax} bond compared with the other models that were for the benzimidazole base. For all four models, the bond indexes for Co–N₂₃ and Co–N₂₂ that are in the five-membered ring with Co are very close in value and likewise for the Co–N₂₄ and Co–N₂₂ that are in the six-membered ring with Co. Model C with the 6-31G(d,p) basis set shows conspicuously higher bond indexes for all the bonds. These latter bond indexes have the largest values of bond index when compared to the models with the 6-311G(d,p) basis set. The Wiberg bond index for the S_{ax}–Co bond is approximately twice that of the other bond indexes in Table 4, indicating that it is much more covalent than the equatorial and axial Co–N bonds, which are dative in character.

Table 5 shows the Wiberg Bond index total by atoms for various models and a comparison of the Mulliken and natural atomic charge for the three types of calculations. The models give similar Wiberg Bond index totals by atoms except that of model F, which shows a higher index for Co. In terms of charge on the atoms, the main difference across the models is that more charge is donated to the Co ion in model F as reflected by the lower charge on the Co both in the Mulliken and natural atomic charge analysis in this calculation. The lower negative charge on the S_{ax} atom also indicates the charge transfer of electron density to the Co.

E. Simulation of the Electronic Absorption and CD Spectrum of GS-Cbl. We compared two types of excited state calculations for each of the three different chemical models of GS-Cbl: GS-Co-corr-Im, zwitterionic GS-Co-corr-Bz, and GS-Co-corr-Bz. As previously outlined, these were with the ground and excited state calculations in vacuum for GS-corrin-Im and calculations where the solvent was taken into account in both the optimization step and the excitation step (solvent optimized) for GS-Co-corr-Im and the two forms of GS-Co-corr-Bz. In addition to the different chemical structural models, we also used both the B3LYP and BP86 density functional methods with the same basis set, 6-311G(d,p), for all calculations. Figure 8 shows the results for five different cases. Four cases are at the B3LYP/6-311G(d,p) level for GS-Co-corr-Im in vacuum and water, zwitterionic GS-Co-corr-Bz, and the protonated form in water. The fifth case is for GS-Co-corr-Bz in water at the BP86/6-311G(d,p) level. The experimental absorption spectrum is included for comparison. The calculation results are for Gaussian broadened (1700 cm^{-1} HWHH) oscillator strengths versus wavelength and have not been energy shifted, although density functional results usually overestimate transition energies. It is seen from the plot that for B3LYP only excitations below 500 nm appear for all the model

Table 5. Wiberg Bond Index (BDIX) Total by Atom and Mulliken (Natural) Atomic Charges^a

atoms	Wiberg BDIX total (A)	Wiberg BDIX total (D)	Wiberg BDIX total (F)	Mulliken (natural) charge (A)	Mulliken (natural) charge (D)	Mulliken (natural) charge (F)
Co	2.73	2.70	3.10	1.26 (1.21)	1.29 (1.26)	1.21 (1.14)
N ₂₃	3.23	3.24	3.30	-0.578 (-0.594)	-0.571 (-0.591)	-0.526 (-0.545)
N ₂₁	3.27	3.28	3.34	-0.544 (-0.548)	-0.549 (-0.546)	-0.505 (-0.505)
N ₂₄	3.28	3.29	3.34	-0.547 (-0.552)	-0.545 (-0.546)	-0.503 (-0.506)
N ₂₂	3.24	3.23	3.29	-0.575 (-0.592)	-0.581 (-0.598)	-0.537 (-0.553)
N _{ax}	3.18	3.19	3.23	-0.440 (-0.558)	-0.533 (-0.571)	-0.511 (-0.542)
S _{ax}	2.02	1.95	2.03	-0.267 (-0.239)	-0.362 (-0.328)	-0.297 (-0.254)

^a(A) GS-Co-corr-Im⁺, B3LYP/6-311G(d,p), vac. (D) GS-Co-corr-Bz⁺, B3LYP/6-311G(d,p), cpcm. (F) GS-Co-corr-Bz⁺, BP86/6-311G(d,p), cpcm.

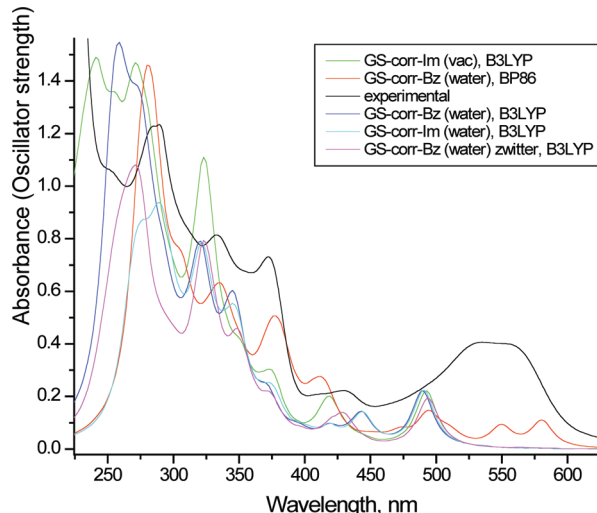


Figure 8. Gaussian broadened (1700 cm^{-1}) oscillator strength vs wavelength in nanometers compared with the experimental absorption spectrum at pH 5.00. The calculation magnitudes have been arbitrarily multiplied by a factor of 6.

systems, while the BP86 calculation has oscillator strength under the first few low energy transitions in the experimental spectrum in the 512 to 600 nm region. This is quite noteworthy since most previous calculations of various cobalamins, especially with the B3LYP functional, needed to be red-shifted by ca. 3000 cm^{-1} to allow plots to match experiment. This is because the hybrid functional usually overestimates the transition energies. In our calculations, the B3LYP results would need to be red-shifted by amounts of between 2475 cm^{-1} and 2605 cm^{-1} for the low energy transition to line-up with the α deconvoluted peak in the experimental spectrum at 561 nm.

The 12 discernible peaks in the experimental absorption spectrum in Figure 8 are listed in Table 6, along with the wavelengths of the Gaussian deconvoluted peaks in this spectrum (The spectral deconvolution is shown in Figure S2). The α,β region can be deconvoluted into five components at 612, 583, 561, 529, and 496 nm. When the four structural models calculated with B3LYP are shifted by the necessary amounts to line up with the 561 nm band (Figure S3 of the Supporting Information), they all show only one or two bands in this region. Likewise, in the B3LYP calculations of Conrad and Brunhold, only two bands are reported in this region.²² The red-shifted peaks in two of these simulated spectra from Gaussian broadened oscillator strength are reported in Table 6. None of the B3LYP or BP86 simulated spectra have a band close to the experimentally observed deconvoluted peak at 529

Table 6. Comparison of Spectral Peaks in Nanometers for GS-Co(III)-corrin-Bz Models Calculated in Water Solvent with the Experimental Absorption Spectrum of GS-Cbl, pH 5

experimentally observed peaks (nm)	deconvoluted peaks (nm) from experiment ^a	protonated GS- peaks (nm) BP86/6-311G(d,p) ^b	protonated GS- peaks (nm) B3LYP/6-311G(d,p) ^c	zwitterionic GS- peaks (nm) B3LYP/6-311G(d,p) ^d
615 sh	612 w	580		
	583 ms			
561	561 ms	555	560	561
534	529 ms			
498	496 m	493	500	501
	479 w	473	472	472
	457 w	449		
433	432 m		441	446
410	408 m	412	411	415
	388 w			
372	375 s	378	380	381
355	357 ms	347		
333	334 vs	337	348	351
310 sh	304 vs	306	315	312
	291 vs			
287	280 s	284	296	295
283	279 s	276		290
	269 s		274	
254	252 vs			

^aDeconvoluted spectrum is shown in Figure S2. Deconvoluted bands - vs: very strong, s: strong, ms: medium strong, m: medium, w: weak.

^bPeaks taken from Figure 8, no shift in calculated peaks. ^cPeaks taken from Figure S2, red-shifted 2605 cm^{-1} . ^dPeaks taken from Figure S2, red-shifted 2545 cm^{-1} .

nm. A deconvoluted experimental band at 535 nm (18700 cm^{-1}) was also reported by Conrad and Brunold.²² In aquocobalamin, this band was considered to be a vibronic band, and therefore the purely electronic excitation calculations do not show this band. We also consider this band in GS-Cbl to be of vibronic origin. If this is a vibronic transition involving the excited state at 561 nm, then the energy splitting between it and 529 nm gives a vibrational energy of 1079 cm^{-1} . There could be a second band in the progression at around 500 nm and a deconvoluted band is found at 496 nm, but this can be assigned as a pure electronic transition. Also the deconvoluted band at 612 nm may also be of vibronic origin, which is further discussed in section F.

The shifted simulations also show that, on comparing the water with the vacuum results for GS-Co-corr-Im, the vacuum calculation does not simulate the experimental band at 496 nm. All the other simulations in water do show a transition around

500 nm. Another indication of the improvement of the solvent optimized calculations over the vacuum one is the simulation in the 330 to 380 nm region. The experimental spectrum shows two strong peaks at 372 and 333 nm with a less resolved band at 355 nm in the valley between them. All of the water calculations suppress oscillator strength in this valley, which is most pronounced at 350 nm in the shifted vacuum calculation. In fact, the BP86 calculation does the best at simulating this region.

Other comparisons of interest from the results in Figure 8 are between the B3LYP water-optimized GS-Co-corr-Im and the B3LYP water-optimized GS-Co-corr-Bz, which are nearly on top of each other. Thus changing the axial base from imidazole to DBz has little effect on the calculated excitation spectra with B3LYP. Also the water optimized zwitterionic and protonated GS-Co-corr-Bz B3LYP shifted simulations are almost exactly equal to each other as seen in Table 6, but the spectrum of the shifted zwitter ion form lacks any features in the 270–280 nm region, which is observed in the experimental spectrum. Both the B3LYP and BP86 water optimized simulations for protonated carboxylic groups do show bands in this region. In comparing the latter two simulations when the B3LYP excitations are red-shifted, most of the calculated peaks are very close in wavelength (Table 6) except that the BP86 calculations show the experimental peak at 580 nm, which is not calculated with B3LYP. Also BP86 does much better in simulating the very strong peak in the experimental spectrum at 333 nm where the shifted B3LYP simulation is nearly 15 nm too low at 348 nm (Table 6).

The electronic position operator oscillator strengths used in Figure 8 were arbitrarily multiplied by a factor of 6 to obtain spectra of the same magnitude as the experimental absorption spectrum. In order to make comparisons on an absolute basis with experiment, we converted these oscillator strengths to molar extinction coefficients using the formula⁸⁶ $f_i = 4.61 \times 10^{-9} \epsilon_{\max} \bar{\nu}_{1/2}$, where $\bar{\nu}_{1/2}$ is the fixed full width at half-maximum (fwhm) for each band. A value of $\nu_{1/2} = 1000 \text{ cm}^{-1}$ was used to convert all oscillator strengths to ϵ_{\max} which were then Lorentzian broadened by 1000 cm^{-1} (fwhm) to simulate the spectrum (Figure 9).

The results in Figure 9 show good absolute agreement of the water optimized BP86/6-311G(d,p) simulated spectrum with the experimental spectrum. Both B3LYP/6-311G(d,p) and BP86/6-311G(d,p) excitation calculations give extinction coefficients that are within a factor of about 2 or better of the experimental extinction coefficients (Figure S4). The oscillator strengths are increasingly overestimated as the transitions move toward higher energies (425 nm to 250 nm region). The B3LYP calculation needed to be uniformly red-shifted by 2605 cm^{-1} to match up (Figure S4), but this is far less than shifts made in previous comparisons of vacuum excitations B3LYP calculations with cobalamin experimental spectra in water. For example, shifts of 5500 cm^{-1} were used for these comparisons in aquo-, methyl-, and adenosyl- cobalamins²⁷ and 3000 cm^{-1} for GS-Cbl simulations.²² It is rather remarkable that the BP86/6-311G(d,p) water calculation is so good at predicting the transition energies. Furthermore, it is clear that the BP86 gives a better simulated spectrum than B3LYP with respect to extinction coefficients and wavelength (Figure S4).

In Figure 10 we compare the experimental and simulated (BP86) CD spectra. The absolute EDC calculated spectrum was compared with the room-temperature experimental

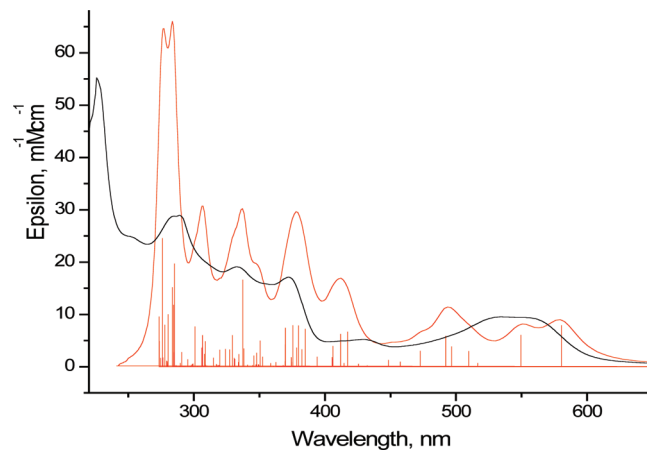


Figure 9. Absolute electronic absorption (extinction) vs wavelength (nm) spectra from a BP86/6-311G(d,p) GS-Co-corr-Bz aqueous model compared with the experimental spectra (black) at pH 5.00, calculated oscillator strength (red sticks), and their Lorentzian broadened (1000 cm^{-1} , fwhm) extinction coefficients spectrum in $\text{mM}^{-1} \text{ cm}^{-1}$ (red line vs wavelength). The conversion of oscillator strength to extinction coefficient maximum is discussed in the text.

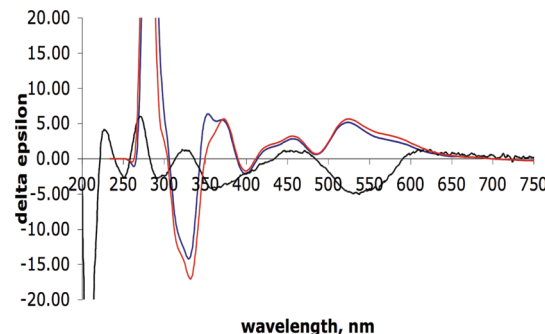


Figure 10. Absolute EDC in units of differential extinction ($\text{M}^{-1} \text{ cm}^{-1}$) vs wavelength (nm) from rotatory strengths. Results were calculated in both length (red) and velocity (blue) gauges, which are Gaussian broadened (1200 cm^{-1} , HW at $1/e$ of peak). The conversion of rotatory strength to differential extinction is discussed in the text.

differential extinction spectrum (black) as shown in Figure 10 by converting calculated rotatory strength to differential extinction. The differential extinction in $\text{M}^{-1} \text{ cm}^{-1}$ is given by⁸⁷ $\Delta\epsilon_i = (\lambda^0 R \times 10^{40} / 22.94 \lambda_{1/2} \sqrt{\pi})$, where R is the calculated rotatory strength for randomly oriented samples in the cgs units of $10^{-40} \text{ erg-esu-cm/Gauss}$, λ^0 is the transition energy (band center in cm^{-1}), and $\lambda_{1/2}$ in cm^{-1} is the half-width at $1/e$ of the peak height. The value of $\lambda_{1/2}$ used to convert to $\Delta\epsilon$ was 1200 cm^{-1} , and the spectrum was broadened with a Gaussian half-width ($1/e$ max) of 1200 cm^{-1} or a fwhm of 1998 cm^{-1} . Both the velocity and length rotatory strengths were compared from the BP86/6-311G(d,p) calculation with experiment. There is well-known problem with all-electron calculations that use Gaussian basis sets in that they do not obey gauge-invariance with finite basis set representations.⁸⁸ Usually the velocity gauge is used, which does alleviate some of this problem. Our results do vary slightly with gauge at each transition energy, but for the most part the two simulated CD spectra are very similar and track each other with a noticeable deviation around 350 nm (Figure 10).

Comparing the absolute experimental and simulated ECD spectra, the magnitude of the differential extinction $\Delta\epsilon$ of the

simulated spectrum agrees quite well with the experimental spectrum, especially in the 350–600 nm region, but again at lower wavelength, the magnitude of the simulated results are substantially larger. In addition, what is immediately obvious in Figure 10 is that $\Delta\epsilon$ calculated for several bands is opposite in sign to the experimental bands. Simulating the experimental ECD spectrum is complicated by the fact that each experimental band can be a summation of rotatory strengths at more than one transition, and simulating the bands depends on how the rotatory strengths are allocated to each band and their bandwidths. Table 7 shows a comparison of the

Table 7. Deconvoluted Peaks and Band Widths from the Experimental GS-Cbl ECD Spectrum Compared with the UV-Vis Spectrum

deconvoluted UV-vis peaks in nm	deconvoluted peak centers in ECD spectrum in nm	ECD peak heights $\Delta\epsilon$ in $M^{-1}cm^{-1}$	fw hm in cm^{-1}
615	608	3.8739	2177.6
561	558	-6.37544	1865.9
529	524	-6.19468	1753.3
496, 475	472	2.83331	2008.1
457, 432	448	1.63826	1113.6
408	405	-1.55219	1218.2
388	381	-3.44911	2206.2
357	357	-6.49011	2667.2
334	327	4.2112	2828.3
304	302	-3.48864	1535.6
291, 280, 279	289	-5.58614	1913.3
269	270	12.1707	2468.7
252	252	-6.26344	2565.2

deconvoluted ECD and UV-vis experimental spectral bands, and it is clear that the transition energies are consistent between the two except that the UV-vis displays more transitions. It is also seen that the ECD bandwidths (fwhm) vary from around 1000 to 2600 cm^{-1} (Table 7). Nonetheless, even with variable bandwidths, it does not seem that the simulated spectrum could be made into a good fit to the experimental one. An explanation for the poor match between experimental and simulated ECD spectra is that the truncated geometric model is not sufficient because it lacks side-chains, which should affect the configuration of the glutathionyl group. It has been found in the X-ray crystal structure study that the GS- ligand could be modeled in two distinct configurations.¹¹ Thus the simulated structure is a good representation of the experimental structure involved in the electronic transitions, but it does not represent the solution configurations to which the ECD spectrum is sensitive.

F. Electronic Transitions from TD-DFT Calculations. In an excited state singlet TD-DFT treatment with the BP86 density functional for the aqueous GS-Co-corr-Bz model, we calculated 100 excited states. Most transitions were calculated in the visible, and the lowest wavelength (highest energy) transition was at 273 nm in the UV region. In contrast, with the B3LYP TD-DFT treatment with the same chemical model, only 50 excited states were needed to get to the highest energy transition at 252 nm. One of the reasons for the good fit of the former calculation is the multitude of transitions calculated in the UV region as seen from Figure 9.

In both BP86 and B3LYP calculations, the HOMO to LUMO transition is calculated with a very low oscillator strength. The calculations with BP86 show a first excited singlet

state, S_1 , at 756.90 nm with oscillator strength $f = 0.0010$, and this is the HOMO \rightarrow LUMO with 0.69 (95%) expansion coefficient. State 2 is at 663.36 nm with an even smaller oscillator strength, $f = 0.0002$, and is the HOMO \rightarrow LUMO+1 with 0.70 (98%) expansion coefficient. Calculated excited states S_1 and S_2 are excited state transitions that are dominated by a simple transition between one OMO and a UMO. In most of the other excited state transitions, several Slater determinants of occupied to vacant orbital promotions make up the excitation. These low intensity transitions do not appear strong enough to come out in the experimental spectrum above 600 nm. However, there is a broad deconvoluted peak (Table 6 and Figure S2) centered at 612 nm, and this transition is also seen in the CD spectrum at 609 nm, but the closest calculated excitation is S_2 at 663 nm. As suggested by a reviewer, this band at 612 nm may be a false origin and vibronic in nature from a vibronic transition to the S_2 excited vibrational state. The energy splitting would put the excited state vibration at 1265 cm^{-1} , which is 230 cm^{-1} lower than the long-axis vibration found by resonance Raman,²² but it could be that the vibration is lowered in the excited state.²⁷ The theoretical BP86 results indicate that the two lowest energy transition are above 600 nm and are very weak. This is consistent with their ill-defined nature in the experimental absorption spectrum in this region.

For the BP86 calculation, we use the compact NTOs of Martin's treatment to discuss the nature of the transitions in the UV-vis absorption spectrum. Table 8 gives the excitation properties of the 34 states with significant oscillator strength ($f \geq 0.01$) in terms of the description of the hole and electron NTOs. Images of the 34 hole and electron isosurfaces are illustrated in Figure S6. We also report in the Supporting Information (Table S2) the set of expansion coefficients for each of these 34 excited states. In the first column of Table 8, we indicate 15 deconvoluted experimental bands to which the calculated excitations can be assigned. We include S_1 as an exception ($f = 0.001$) in the tables since it is the HOMO \rightarrow LUMO transition. In this transition, the electron density change is mainly from the Spy \rightarrow corr π^* , but the NTOs also show that a small amount of electron density goes from an extended σ bond (N24–Co(dy_z)-N22)⁸⁹ to the corr π^* leaving Co(dy_z) occupation in the electron NTO. Other stronger transitions that include the HOMO in the hole where the sulfur p_y orbital is a major contributor of electron density are S_8 , S_{27} , and S_{40} , where the expansion coefficients (Table S2) that contain the HOMO in the donor are 55%, 74%, and 96%, respectively. Moreover, Table 8 shows that almost every transition contains cobalt d orbitals in the hole and electron NTOs. This can be seen in the snap shots of the NTO hole-electron isosurfaces of the excitations (Figure S6).

The first calculated state with strong oscillator strength, $f = 0.0337$, is S_3 at 580.50 nm and is the only excitation that appears under the deconvoluted peak at 583 nm of the experimental spectrum (Figure 9 and Table 8). This transition contains two parts: (i) a localized axial σ Co(dz₂)-S(p_z) bond \rightarrow Co(dy_z) atomic orbital and (ii) a corr $\pi \rightarrow$ corr π^* . This transition is the HOMO-1 \rightarrow LUMO transition (Table S2) with an expansion coefficient is 93%. In part (i), it appears that electron density comes out of the hole σ bond leaving a bare Co(dy_z) orbital in the excited state in addition to corrin π^* orbitals (Figure 11). The next excited state transition S_4 at 560.6 nm also has considerable oscillator strength ($f = 0.0257$) as noted in Table 8 and again is the only transition under the deconvoluted peak at 561 nm. Table S2 shows this transition is

Table 8. NTOs for Hole and Electron Isosurfaces from a BP86/6-311(d,p) Calculation That Are Correlated with Deconvoluted Bands in the Experiment Absorption Curve of Gluthionylcobalamin

band	state	E (eV)	λ (nm)	f	hole	electron
	1	1.638	756.9	0.001	$\sigma(\text{Neq}-\text{Co}(\text{dyz})-\text{Neq}) + \text{Spy}$	$\text{Co}(\text{dyz}^*) + \text{corr } \pi^*$
583	3	2.1358	580.5	0.0337	$\sigma(\text{Co}(\text{dz2})+\text{S}(\text{pz})) + \text{corr } \pi + \text{Nax}(\text{pz})$	$\text{Co}(\text{dyz}^*) + \text{corr } \pi^*$
561	4	2.2562	549.52	0.0257	$\sigma(\text{Co}(\text{dz2})+\text{S}(\text{pz})) + \text{corr } \pi + \text{Nax}(\text{pz})$	$\text{Co}(\text{dz2}^*) + \text{S}(\text{pz})^* + \text{Nax}(\text{pz})^* + \text{corr } \pi^*$
496	6	2.4321	509.79	0.0125	$\sigma(\text{Co}(\text{d2z})+\text{Spy}) + \text{Bzm } \pi + \text{corr } \pi$	$\text{Co}(\text{dyz}^*) + \text{corr } \pi^*$
	8	2.4962	496.7	0.0162	$\text{Co}(\text{dyz}) + \text{S}(\text{py})$	$\text{Co}(\text{dxz}^*) + \text{corr } \pi^*$
	9	2.519	492.2	0.025	$\pi(\text{Co}(\text{dyz})+\text{S}(\text{pz})+\text{corr } \pi)$	$\text{Co}(\text{dx2-y2}^*) + \text{S}(\text{pz}^*) + \text{corr } \pi^*$
475	10	2.6228	472.72	0.0128	$\text{Co}(\text{dz2}) + \text{corr } \pi + \text{Bzm } \pi$	$\text{Co}(\text{dz2}^*) + \text{S}(\text{pz}^*) + \text{Neq}^* + \text{Nax}(\text{pz})^*$
456	12	2.7643	448.53	0.0052	$\sigma(\text{Co}(\text{dxz})+\text{S}(\text{pz})) + \text{corr } \pi$	$\text{Co}(\text{dx2-y2}^*) + \text{corr } \pi^*$
408	18	2.9705	417.39	0.0283	$\sigma(\text{Co}(\text{dxz})+\text{S}(\text{pz})+\text{Nax}(\text{pz})) + \text{gluO}(\text{py}) + \text{Bzm } \pi$	$\text{Co}(\text{dyz}^*) + \text{corr } \pi^*$
	20	3.0084	412.13	0.0266	$\sigma(\text{dz2}+\text{Spz}) + \text{corr } \pi + \text{Nax}(\text{pz})$	$\text{Co}(\text{dxz}^*) + \text{corr } \pi^*$
	21	3.0531	406.1	0.0167	$\pi(\text{Co}(\text{dxz}) + \text{Nax}(\text{px})) + \text{glu} + \text{Bzm } \pi$	$\text{Co}(\text{dz2}^*) + \text{S}(\text{pz})^* + \text{Nax}(\text{pz})^* \text{ corr } \pi^*$
388	24	3.2196	385.09	0.0307	$\pi(\text{Co}(\text{dyz})+\text{S}(\text{py})) + \text{corr } \pi$	$\text{Co}(\text{dx2-y2}^*) + \text{corr } \pi^*$
375	25	3.2414	382.5	0.0139	$\sigma(\text{Co}(\text{dz2})+\text{S}(\text{pz})) + \text{Nax}(\text{pz}) + \text{corr } \pi$	$\text{Co}(\text{dx2-y2}^*) + \text{Bzm } \pi^*$
	26	3.2639	379.86	0.0335	$\pi(\text{Co}(\text{dyz})+\text{S}(\text{py})) + \text{corr } \pi$	$\text{Co}(\text{dxz}^*) + \text{corr } \pi^*$
	27	3.2756	378.5	0.0154	$\text{Co}(\text{dyz}) + \text{S}(\text{py})$	$\text{Co}(\text{dx2-y2}^*) + \text{corr } \pi^*$
	29	3.301	375.59	0.0338	$\sigma(\text{Co}(\text{dxy})+\text{S}(\text{pz})) + \text{glu}$	$\text{Co}(\text{dz2}^*) + \text{S}(\text{pz}^*) + \text{Nax}(\text{pz}^*)$
	31	3.3527	369.81	0.0316	$\text{Co}(\text{dxy}) + \text{S}(\text{px}) + \text{corr } \pi + \text{glu}$	$\text{Co}(\text{dz2}^*) + \text{S}(\text{pz}^*) + \text{Nax}(\text{pz}^*)$
357	37	3.5367	350.56	0.021	$\sigma(\text{Co}(\text{dx2-y2})+\text{S}(\text{pz}) + \text{Nax}(\text{pz})) + \text{corr } \pi$	$\text{Co}(\text{dyz}^*) + \text{S}(\text{pz}^*) + \text{Nax}(\text{pz}^*) + \text{corr } \pi^*$
	40	3.5632	347.96	0.0111	$\text{Co}(\text{dyz}) + \text{S}(\text{py})$	$\text{Glu } \pi^*$
330	46	3.6739	337.47	0.071	$\pi(\text{Co}(\text{yz})+\text{S}(\text{py})) + \sigma(\text{Co}(\text{dyz})+\text{Neq}) + \text{corr } \pi$	$\text{Co}(\text{dyz}) + \text{corr } \pi^*$
	52	3.7623	329.54	0.0255	$\text{Co}(\text{dxy}) + \text{corr } \pi$	$\text{Co}(\text{dx2-y2}^*) + \text{Bzm } \pi^* + \pi(\text{Neq} + \text{C}(\text{pz}))$
304	64	4.0155	308.76	0.0206	$\pi(\text{Co}(\text{dxz})+\text{S}(\text{px})) + \text{glu}$	$\text{Co}(\text{dxz}^*) + \text{corr } \pi^*$
	66	4.0418	306.75	0.0256	$\pi(\text{Co}(\text{dyz})+\text{S}(\text{py})) + \text{corr } \pi$	$\text{Co}(\text{dx2-y2}^*) + \text{corr } \pi^*$
	67	4.0442	306.58	0.0164	$\text{Co}(\text{dxz}) + \text{glu}$	$\text{Co}(\text{dx2-y2}^*) + \text{Neq}(\text{sp}2^*)$
	71	4.1205	300.89	0.0326	$\text{Co}(\text{dxz}) + \text{corr } \pi + \text{Bzm }$	$\text{Co}(\text{dx2-y2}^*) + \text{corr } \pi^*$
296	85	4.3481	285.15	0.0842	$\pi(\text{Co}(\text{dyz})+\text{S}(\text{py})) + \text{corr } \pi$	$\text{Glu } \pi^*$
	88	4.3554	284.67	0.0505	$\pi(\text{Co}(\text{dyz})+\text{S}(\text{py})) + \pi(\text{Co}(\text{dyz})+\text{Neq}(\text{pz})) + \text{corr } \pi$	$\text{Co}(\text{dxy}^*) + \text{Neq}(\text{sp}2^*) + \text{glu } \pi^*$
	89	4.3722	283.57	0.0648	$\sigma(\text{Co}(\text{dz2})+\text{S}(\text{pz})) + \text{Nax}(\text{pz}) + \text{corr } \pi$	$\text{Co}(\text{dy2}^*) + \text{S}(\text{pz}^*) + \text{Nax}(\text{py}^*) + \text{corr } \pi^*$
280	90	4.4213	280.43	0.0426	$\pi(\text{Co}(\text{dyz})+\text{S}(\text{py})) + \pi(\text{Co}-\text{Neq}(\text{pz})) + \text{corr } \pi$	$\text{Co}(\text{dxz}^*) + \text{corr } \pi^*$
279	93	4.46	277.99	0.0341	$\pi(\text{Co}(\text{dyz})+2\text{Neq}) + \text{corr } \pi$	$\text{Co}(\text{dyz}^*) + \text{corr } \pi^*$
269	96	4.4888	276.21	0.105	$\sigma(\text{Co}(\text{dz2})+\text{S}(\text{pz})) + \text{Bzm } \pi$	$\sigma^*(\text{Co}(\text{dz2}^*) + \text{S}(\text{pz}^*)) + \text{Nax}(\text{px}^*) + \text{corr } \pi^*$
	97	4.4897	276.15	0.0302	$\text{Glu O}(\text{py})$	$\sigma^*(\text{Co}(\text{dz2}^*) + \text{S}(\text{pz}^*)) + \text{Nax}(\text{pz}^*) + \text{Neq}(\text{px}^*)$
	99	4.5273	273.86	0.0208	$\text{Co}(\text{dx2-y2}) + \text{glu}$	$\text{Co}(\text{dxy}) + \text{corr } \pi^*$
	100	4.5313	273.62	0.0406	$\text{Co}(\text{dyz}) + \text{corr } \pi + \text{Bzm } \pi$	$\text{Co}(\text{dz2}^*) + \text{S}(\text{pz}^*) + \text{corr } \pi^*$

a HOMO-1 → LUMO+1 transition with an expansion coefficient of 86%. These transitions, S_3 and S_4 , contain $\pi \rightarrow \pi^*$ corrin ring and also a $\sigma(\text{Co-S}) \rightarrow \text{Co(d)}$ type transition. The electron and hole NTOs for the two transitions are shown in Figure 11. Other transitions that involve the Co-S σ bond in the hole are S_{18} , S_{20} , S_{25} , S_{37} , and S_{89} .

There are also a number of transitions that clearly show the Co-S π bonding interaction in the hole. For example, excited state 24 ($f = 0.0307$), which can be assigned to the deconvoluted band at 388 nm can again be decomposed into two components: $\pi(\text{Co}(\text{dyz})+\text{S}(\text{py})) \rightarrow \text{Co}(\text{dxz}^*)$ and $\text{corr } \pi \rightarrow \text{corr } \pi^*$, which is shown in the hole and electron NTOs for S_{24} (Figure 12). The hole NTO for S_{24} contains HOMO-2 (Figure 6), which shows π Co-S bonding and comes from an expansion coefficient that contributes 44% of the transition. Other excited states where the hole NTO shows a π Co-S bonding interaction (Table 8 and Figure S6) are S_9 ($f = 0.025$), S_{26} ($f = 0.0335$), S_{66} ($f = 0.256$), and S_{85} ($f = 0.0842$), which are dominated by HOMO-2 in the donor with 52%, 44%, 42%, and 62%, expansion coefficient contributions, respectively. The strongest oscillator strength of any transition is for S_{85} , and the hole and electron NTOs are also shown in Figure 12, where the overall transition is $\pi(\text{Co}(\text{dyz})+\text{S}(\text{py})) + \text{corr } \pi \rightarrow$ glutamacyl part of the glutathionyl axial ligand.

There are quite a few excited states in which the hole NTOs show a complicated isosurface involving more than simple Co-S bonding and/or corrin π bonds. For example, excited state 46 ($f = 0.071$) assigned to the band at 357 nm and excited state 90 ($f = 0.0426$) assigned to the band at 280 nm are both excitations with considerable oscillator strength and have multicentered donors. Figure 13 clearly shows that the hole NTO for S_{46} has a four-centered Neq-Co-S-Neq bonding interaction from which density is withdrawn and donated to $\text{Co}(\text{dyz})$ and corrin π^* in electron NTO. On the other hand, excited state S_{90} has a five-centered bonding interaction involving Co and all four pyrrole ring Neq atoms and the S(py) with $\pi(\text{Co}(\text{dyz}))\text{-S}(\text{py})$ and $\pi(\text{Co}-\text{Neq})$ bonding from which density is withdrawn and donated to $\text{Co}(\text{dxz}^*)$ and corrin π^* in electron NTO as is seen in Figure 13. This hole NTO exhibits the utility of the NTO analysis of electronic excitations since nine MOs contribute to the donor of excited state 90 with contributions of only 3% to 15% for any one MO, making it impossible to understand this transition from a MO analysis.

IV. SUMMARY AND CONCLUSIONS

We have used DFT and TD-DFT calculations to analyze geometry, bonding, and electronic transitions and to simulate

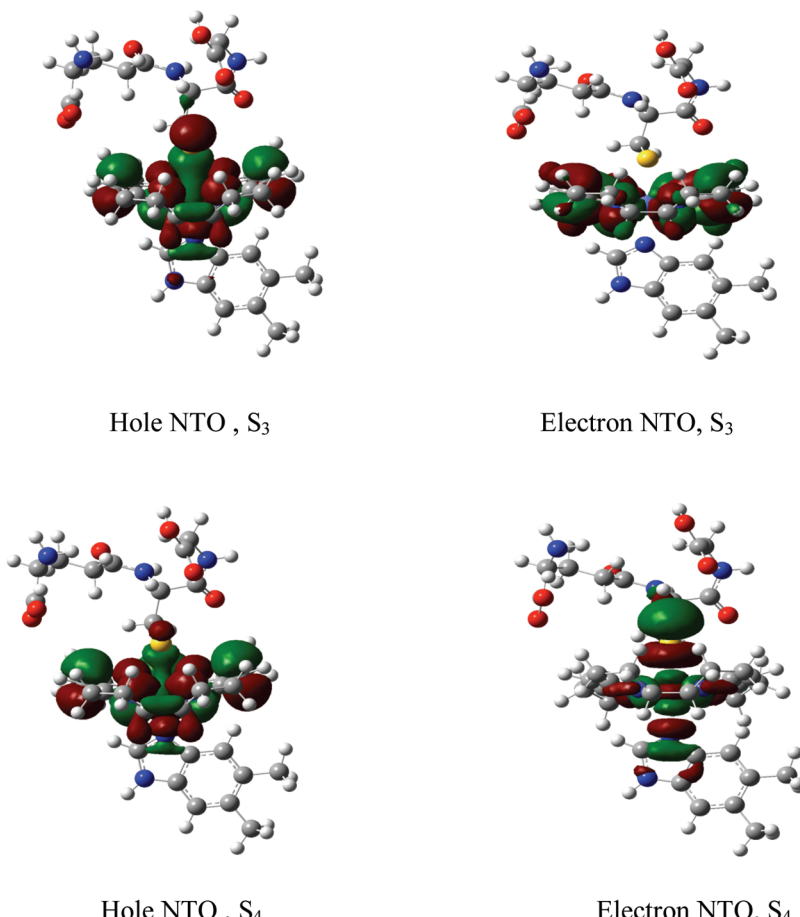


Figure 11. Electron and hole isosurfaces of NTOs for states S_3 and S_4 from a BP86/6-311(d,p) calculation.

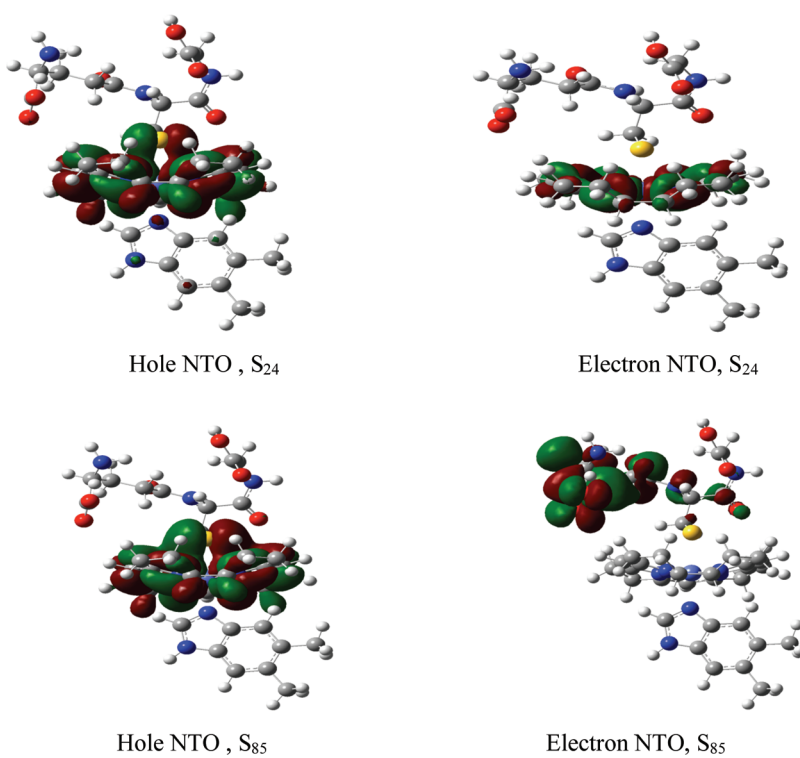


Figure 12. Electron and hole isosurfaces of NTOs for states S_{24} and S_{85} from a BP86/6-311(d,p) calculation.

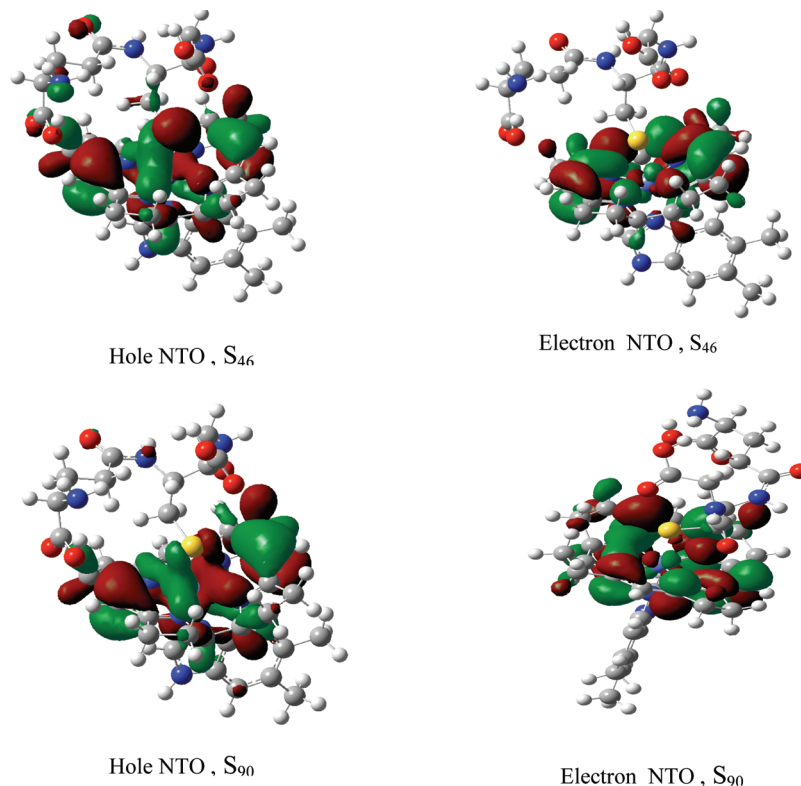


Figure 13. Electron and hole isosurfaces of NTOs for states S_{46} and S_{90} from a BP86/6-311(d,p) calculation.

UV-vis and ECD spectra of the biologically important GS-Cbl molecule. Although the truncated chemical model does not contain the methyl, amide, and nucleotide side chains, the geometry optimization results give highly accurate values for the Co-corrin ring with axial ligands. Variation of conditions such as the axial base (imidazole for DBz), water versus vacuum calculation, and zwitter ion versus protonated structure of the glutathionyl ligand did not affect the main geometric features of the chemical model. The geometric optimizations accurately reflect the structural features of glutathionyl-cobalamin such as the axial and equatorial cobalt-ligand bond distances and the fold angle. Geometric optimizations made in vacuum show a better fit to the X-ray crystal structure with respect to bond distances which may reflect the real differences between the solid and solution states.

In terms of the chemical bonding and electronic excitations, the BP86 DFT functional yielded more π Co–S bonding features and also shows more participation of d orbitals of Co in the electronic transitions than the B3LYP hybrid functional. Evidence for π bonding in Co–S comes from the BP86 MO isosurfaces, which shows this bonding interaction. The latter observation was recently stressed by Kozlowski and co-workers.⁹⁰ The ECDA from AOMIX shows that the Co–S bond in GS-Cbl is formed by substantial charge transfer of 0.785 electron compared to 0.802 for the Co–C bond in Me-Cbl in the vacuum BP86 calculation. This result and the similarity of the Mayer bond orders for Co–S in the GS-Cbl model in comparison to Co–C in a Me-Cbl model shows the covalent character of the bond. This is in agreement with the conclusion of Conrad and Brunold.²²

The NBO analysis gives a picture of the metal–ligand bonding interactions in the coordination sphere of the molecule. A detailed NBO donor–acceptor analysis, which we have not included herein, shows the formation of ω

hypervalent bonds. The Co-ligand axial and equatorial bonds show the strong collinearity that is characteristic of these 3c/4e bonds.⁸³ In the NBO analysis with B3LYP, the basis set, 6-311G(d,p) or 6-31G(d,p), had the effect of changing the ideal NHO on Co from sd^2 to sp^3d^2 in the NBO σ bond formation. The bonding from the NBO analysis in the Co ligand structure of GS-Cbl is consistent with an 18 electron system with three lone pair d orbitals almost fully occupied. Thus the electron sum comes from six electrons in three lone pair Co d orbitals and 12 electrons in the Co-ligand bonds, which are formed by charge donation from the ligands to Co unoccupied orbitals. The 12 electrons are in the σ bonds formed across two collinear N_{eq} –Co– N_{eq} and one collinear S_{ax} –Co– N_{ax} bonds. Here the dative bonding equatorial and axial nitrogen ligands show up as sp^2 or sp^3 NHOs with the bond polarized toward the nitrogen. On the other hand, the polarization coefficients for the NBO σ Co– S_{ax} bond show that this bond is more covalent and the NHO involves a pure p_z orbital on the sulfur.

In simulating electronic spectra, calculations with BP86 were more accurate than those with B3LYP. Also, the water cpcm model was clearly superior to the vacuum calculations. We found that the BP86/6-311(d,p) in water calculations gave a much better fit to the spectra than the B3LYP/6-311(d,p) in water with respect to absolute intensity and absolute energy. These results are consistent with those of Kornobis et al.⁹⁰ who found by extensive benchmark analysis that the BP86 functional is more appropriate than the B3LYP functional for describing the electronic properties of cobalamins. We also concluded that the experimental deconvoluted bands at 612 and 529 nm may be vibronic bands; however, more analyses of the spectrum including Franck–Condon and Herzberg–Teller vibronic analysis is necessary for definitive assignments. With regard to the ECD spectrum, it can be concluded that a more complete chemical model involving the side-chains is necessary

to simulate a better fit to the differential extinction experimental results. Finally, the nature of the electronic transitions and the bonding in this macrocyclic metal complex can be most properly illustrated using the hole and electron NTO representation of Martin.⁶⁹ These NTOs show that many transitions can only be depicted by multicentered processes.

■ ASSOCIATED CONTENT

S Supporting Information

Tables for comparison of structure from model calculation with X-ray structure data, for the expansion coefficients and transition from excited state BP86 calculations, and for the partial and total DOS in B3LYP GS-Cbl-Im model calculation. Figures for the Gaussian deconvolution of bands in the experimental absorption spectrum, for comparison of shifted simulations of various models from the B3LYP calculation with the absorbance spectra, for the comparison of B3LYP and BP86 absolute simulated spectra with the experimental absorbance spectrum, for isosurfaces of 25 MOs from the BP86 calculation, and for isosurfaces for 34 hole and electron NTOs from the BP86 calculation. This material is available free of charge via the Internet at <http://pubs.acs.org>.

■ AUTHOR INFORMATION

Notes

The authors declare no competing financial interest.

■ ACKNOWLEDGMENTS

We would like to thank Professor John R. Lombardi for helpful discussions concerning this work. This work was supported in part by a NASA sub-Grant from an SBIR made to Radiation Monitoring Devices, Inc., by two grants from the City University of New York PSC-CUNY Faculty Research Award Program (61632-00 39, 64513-00 42). Computer facilities for this research were supported by Teragrid Grants TG-CHE080072 and TG-CHE090043 and by the CUNY High Performance Computer Center, HPCUNY.

■ REFERENCES

- (1) Wagner, F.; Bernhauer, K. *Ann. N.Y. Acad. Sci.* **1964**, *112*, 580.
- (2) Alder, N.; Medwick, T.; Poznanski, T. *J. J. Am. Chem. Soc.* **1966**, *88*, 5018–5020.
- (3) (a) Pezacka, E.; Green, R.; Jacobsen, D. W. *Biochem. Biophys. Res. Commun.* **1990**, *169*, 443. (b) Pezacka, E. H.; Green, R.; Jacobsen, D. W. *FASEB J.* **1990**, *4*, A2126. (c) Pezacka, E. H.; Jacobson, D. W.; Luce, K.; Green, R. *Biochem. Biophys. Res. Commun.* **1992**, *184*, 832–839. (d) Pezacka, E. H. *Biochim. Biophys. Acta* **1993**, *1157*, 167–177 and references therein.
- (4) Jacobsen, D. W.; Lee-Denison, C.; Luce, K.; Green, R. *Fed. Proc.* **1987**, *46*, 1005.
- (5) (a) Brasch, N. E.; Hsu, T. C.; Doll, K. M.; Finke, R. G. J. *Inorg. Biochem.* **1999**, *76*, 197–209. (b) Suto, R. K.; Brasch, N. E.; Anderson, O. P.; Finke, R. G. *Inorg. Chem.* **2001**, *40*, 2686–2692. (c) Xia, L.; Cregan, A. G.; Berben, L. A.; Brasch, N. E. *Inorg. Chem.* **2004**, *43*, 6848–6857.
- (6) (a) Zhao, R.; Lind, J.; Merényi, G.; Eriksen, T. E. *J. Chem. Soc., Perkin Trans. 2* **1997**, 569. (b) Griffin, O. W. *Free Radical Biol. Med.* **1999**, *27* (9–10), 922–935.
- (7) Brown, K. L.; Zou, X.; Savon, S. R.; Jacobsen, D. W. *Biochemistry* **1993**, *32*, 8421.
- (8) Scheuring, E. M.; Sagi, I.; Chance, M. R. *Biochemistry* **1994**, *33*, 6310.
- (9) Randaccio, L.; Geremia, S.; Nardin, G.; Slouf, M.; Srnova, I. *Inorg. Chem.* **1999**, *38*, 4087–4092.
- (10) Suto, R. K.; Brasch, N. E.; Anderson, O. P.; Finke, R. G. *Inorg. Chem.* **2001**, *40*, 2686.
- (11) Hannibal, L.; Smith, C. A.; Jacobsen, D. W. *Inorg. Chem.* **2010**, *49*, 9921–9927.
- (12) Hsu, T.-L. C.; Brasch, N. E.; Finke, R. G. *Inorg. Chem.* **1998**, *37*, 5109. (b) Brasch, N. E.; Hsu, T.-L. C.; Doll, K. M.; Finke, R. G. *J. Inorg. Biochem.* **1999**, *76*, 197. (c) Suarez-Moreira, E.; Hannibal, L.; Smith, C. A.; Jacobsen, Brasch, N. E. *Dalton Trans.* **2006**, 5269–5277.
- (13) Ngandu, L.; Robin, D.; El Kasmi, A.; Lexa, D. *Inorg. Chim. Acta* **1999**, *292*, 204.
- (14) Watson, P.; Munter, T.; Golding, B. T. *Chem. Res. Toxicol.* **2004**, *17*, 1562–1567.
- (15) Zheng, D.; Birke, R. L. *J. Am. Chem. Soc.* **2002**, *124*, 9066–9067.
- (16) (a) Zheng, D.; Birke, R. L. *J. Am. Chem. Soc.* **2001**, *123*, 4637–4638. (b) Wolak, M.; Zahl, A.; Schneppenensier, T.; Stochel, G.; van Eldik, R. *J. Am. Chem. Soc.* **2001**, *123*, 9780–9791.
- (17) (a) Wheately, C. J. *Nutr. Environ. Med.* **2007**, *16*, 181–211. (b) Wheately, C. J. *Nutr. Environ. Med.* **2007**, *16*, 212–226.
- (18) Weinberg, J. B.; Chen, Y.; Jiang, N.; Beasley, B. E.; Salerno, J. C.; Ghosh, D. K. *Free Radical Biol. Med.* **2009**, *46*, 1626–1632.
- (19) (a) Macaddon, A.; Davies, G.; Hudson, P.; Andy, S.; Cattell, H. *Int. J. Geriatr. Psychiatry* **1998**, *13*, 235–239. (b) Clarke, R.; Smith, A. D.; Jobst, K.; Refsum, H.; Sutton, L.; Ueland, P. M. *Arch. Neurol.* **1998**, *55*, 1449–1455.
- (20) Macaddon, A.; Regland, B.; Hudson, P.; Davies, G. *Neurology* **2002**, *58*, 1395–1399.
- (21) Birch, C. S.; Brasch, N. E.; McCaddon, A.; Williams. *Free Radical Biol. Med.* **2009**, *47*, 184–188.
- (22) Conrad, K. S.; Brunhold, T. C. *Inorg. Chem.* **2011**, *50*, 8755–8766.
- (23) Firth, R. A.; Hill, H. A. O.; Pratt, J. M.; Williams, R. J. P.; Jackson, W. R. *Biochemistry* **1967**, *6*, 2178–2189.
- (24) Pratt, J. M. *Inorganic Chemistry of Vitamin B₁₂*; Academic Press: London, 1972; Chapter 5, pp 44–67.
- (25) Pratt, J. M. In *Chemistry and Biochemistry of B₁₂*; Banerjee, R., Ed.; Wiley: New York, 1999; pp 113–164.
- (26) Salma, S.; Spiro, T. G. *J. Raman Spectrosc.* **1977**, *6*, 57–60.
- (27) Stich, T. A.; Brooks, A. J.; Buan, N. R.; Brunold, T. C. *J. Am. Chem. Soc.* **2003**, *125*, 5897–5914.
- (28) Solomon, E. I.; Gorelsky, S. I.; Dey, A. J. *Comput. Chem.* **2006**, *27*, 1415–1428.
- (29) Day, P. *Theor. Chim. Acta* **1967**, *7*, 328.
- (30) Offenhartz, P. O.; Offenhartz, B. H.; Mel Fung, M. *J. Am. Chem. Soc.* **1970**, *92*, 2966–2973.
- (31) Salem, L.; Eisenstein, O.; Anh, N. T.; Burgu, H. B.; Devaquet, A.; Segal, G.; Veillard, A. *Nouv. J. Chim.* **1977**, *1*, 335.
- (32) Andruniow, T.; Zgierski, M. Z.; Kozlowski, P. M. *J. Phys. Chem. B* **2000**, *104*, 10921–10927.
- (33) Andruniow, T.; Zgierski, M. Z.; Kozlowski, P. M. *J. Am. Chem. Soc.* **2001**, *123*, 2679–2680.
- (34) Jensen, P.; Ryde, U. *J. Phys. Chem. A* **2003**, *107*, 7539–7545.
- (35) Selcuki, C.; van Eldik, R.; Clark, T. *Inorg. Chem.* **2004**, *43*, 2828–2833.
- (36) (a) Dolker, N.; Maseras, F.; Liedos, A. *J. Phys. Chem. B* **2001**, *105*, 7564. (b) Dolker, N.; Maseras, F.; Liedos, A. *J. Phys. Chem. B* **2003**, *107*, 306–315. (c) Jensen, P.; Ryde, U. *J. Mol. Struct.* **2002**, *585*, 239–255.
- (37) Andruniow, T.; Zgierski, M. Z.; Kozlowski, P. M. *Chem. Phys. Lett.* **2000**, *331*, 509–512.
- (38) Jensen, K. P.; Sauer, S. P. A.; Liljefors, T.; Norrby, P.-O. *Organometallics* **2001**, *20*, 550–556.
- (39) (a) Andruniow, T.; Zgierski, M. Z.; Kozlowski, P. M. *Chem. Phys. Lett.* **2000**, *331*, 502–518. (b) Andruniow, T.; Zgierski, M. Z.; Kozlowski, P. M. *J. Phys. Chem. A* **2002**, *106*, 1365–1373.
- (40) Kozlowski, P. M.; Andruniow, T.; Jarzecki, A. A.; Zgierski, M. Z.; Spiro, T. G. *Inorg. Chem.* **2006**, *45*, 5585–5590.
- (41) Stich, T. A.; Buan, N. R.; Brunold, T. C. *J. Am. Chem. Soc.* **2004**, *126*, 9735–9749.

- (42) Liptak, M. D.; Fleisschacker, A. S.; Mathews, R. G.; Telser, J.; Brunold, T. C. *J. Phys. Chem. A* **2009**, *113*, 5245–5254.
- (43) Jaworska, M.; Lodowski, P. *J. Mol. Struct. (THEOCHEM)* **2003**, *631*, 209–223.
- (44) Jensen, K. P. *J. Phys. Chem. B* **2005**, *109*, 10505–10512.
- (45) Liptak, M. D.; Brunold, T. C. *J. Am. Chem. Soc.* **2006**, *128*, 9144–9156.
- (46) Rovira, C.; Blarnés, X.; Kunc, K. *Inorg. Chem.* **2004**, *43*, 6628–6632.
- (47) Jensen, K. P.; Ryde, U. *Coord. Chem. Rev.* **2009**, *253*, 769–778.
- (48) Kuta, J.; Patchkovskii, S.; Zgierski, M.; Kozlowski, P. M. *J. Comput. Chem.* **2006**, *27*, 1429–1437.
- (49) Kuta, J.; Wuerges, J.; Randaccio, L.; Kozlowski, P. M. *J. Phys. Chem. A* **2009**, *113*, 11604–11612.
- (50) Randaccio, L.; Geremia, S.; Stener, M.; Tooffoli, D.; Zangrandi, E. *Eur. J. Inorg. Chem.* **2002**, *93*–103.
- (51) Kurmaev, E. Z.; Moewes, A.; Ouyang, L.; Randaccio, L.; Rulis, P.; Ching, W. Y. *Europhys. Lett.* **2003**, *62*, 582–587.
- (52) Ouyang, L.; Randaccio, L.; Rulis, P.; Kurmaev, E. Z.; Moewes, A.; Ching, W. Y. *J. Mol. Struct.* **2003**, *622*, 221–227.
- (53) Ouyang, L.; Rulis, P.; Ching, W. Y.; Nardin, G.; Randaccio, L. *Inorg. Chem.* **2004**, *43*, 1235–1241.
- (54) Andruniow, T.; Kozlowski, P. M.; Zgierski, M. *J. Chem. Phys.* **2001**, *115*, 7522–7533.
- (55) Brooks, A. J.; Valsie, N. R.; Banerjee, R.; Brunold, T. C. *J. Am. Chem. Soc.* **2004**, *126*, 8167–8180.
- (56) Andruniow, T.; Jaworska, M.; Lodowski, P.; Zgierski, M. Z.; Dreos, R.; Randaccio, L.; Kozlowski, P. M. *J. Chem. Phys.* **2008**, *129*, 085101–1–14.
- (57) Solheim, H.; Kornblis, K.; Ruud, K.; Kozlowski, P. M. *J. Phys. Chem. B* **2010**, *113*, 737–748.
- (58) Lodowski, P.; Jaworska, M.; Andruniow, T.; Kumar, M.; Kozlowski, P. M. *J. Phys. Chem. B* **2009**, *113*, 6898–6909.
- (59) Frisch, M.J.; Trucks, G.W.; Schlegel, H.B.; Scuseria, G.E.; Cheeseman, M.A.; Montgomery, J.A.; Jr., Vreven, T.; Kudin, K.N.; Burant, J.C.; Millam, J.M.; S.S., Martin, D.J. Fox, T. et al. *Gaussian 03*, revision C.02; Gaussian, Inc.: Wallingford, CT, 2004.
- (60) Frisch, M. J.; Trucks, G. W.; Schlegel, H. B.; Scuseria, G. E.; Robb, M. A.; Cheeseman, J. R.; Scalmani, G.; Barone, V.; Mennucci, B.; Petersson, G. A. et al. *Gaussian 09*, revision A.1; Gaussian, Inc.: Wallingford, CT, 2009.
- (61) Tomasi, J.; Mennucci, B.; Cammi, R. *Chem. Rev.* **2005**, *105*, 2999–3093.
- (62) Casida, M. E. In *Recent Advances in Density Functional Methods*; Chong, D. P., Ed.; World Scientific Publishing Co.: Singapore, 1995; Part I, Chapter 5, p 155.
- (63) Hay, P. J.; Wadt, W. R. *J. Chem. Phys.* **1984**, *82*, 299.
- (64) Becke, A. D. *J. Chem. Phys.* **1993**, *98*, 5648.
- (65) Stephens, P. J.; Devlin, F. J.; Chabalowski, C. F.; Frisch, M. J. *J. Phys. Chem.* **1994**, *98*, 11623.
- (66) Becke, A. D. *Phys. Rev. A* **1988**, *38*, 3098–3100.
- (67) Perdew, J. P. *Phys. Rev. B* **1986**, *33*, 8822–8824.
- (68) Gorelsky, S. I. AOMIX version 6.46; Department of Chemistry, York University: Toronto, ON, 2009; <http://www.sg-chem.net>.
- (69) Martin, R. L. *J. Chem. Phys.* **2003**, *118*, 4775.
- (70) Rabenstein, D. L. *J. Am. Chem. Soc.* **1973**, *95*, 2797–2803.
- (71) Brown, K. L. *Chem. Rev.* **2005**, *105*, 2075.
- (72) Randaccio, L.; Geremia, S.; Nardin, G.; Wurergus, J. *Coord. Chem. Rev.* **2006**, *250*, 1332–1350.
- (73) Martin, B. M.; Finke, R. G. *J. Am. Chem. Soc.* **1990**, *112*, 2419.
- (74) Martin, B. M.; Finke, R. G. *J. Am. Chem. Soc.* **1992**, *114*, 585–592.
- (75) Kozlowski, P. M.; Zgierski, M. Z. *J. Phys. Chem. B* **2004**, *108*, 14163–14170.
- (76) Kitaura, K.; Morokuma, K. *Int. J. Quantum Chem.* **1976**, *10*, 325–340.
- (77) Ziegler, T.; Rauk, A. *Theoret. Chim. Acta* **1977**, *46*, 1–10.
- (78) Gorelsky, S. I.; Ghosh, S.; Solomon, E. I. *J. Am. Chem. Soc.* **2006**, *128*, 278–290.
- (79) Dapprich, S.; Frenking, G. *J. Phys. Chem.* **1995**, *99*, 9352–9362.
- (80) Frenking, G.; Fröhlich, N. *Chem. Rev.* **2000**, *100*, 717–774.
- (81) Mayer, I. *Chem. Phys. Lett.* **1983**, *97*, 270–274.
- (82) Glendening, J. K. Badenhoop, A. E. ReedJ. E. Carpenter, J. A. Bohmann, C. M. Morales, Weinhold, F. *NBO 5.9. E. D.*; Theoretical Chemistry Institute, University of Wisconsin: Madison, WI, 2009.
- (83) Weinhold, F.; Landis, C. *Valency and Bonding: A Natural Bond Orbital Donor–Acceptor Perspective*; Cambridge University Press: Cambridge, U.K., 2005.
- (84) Ballhausen, C. J.; Gray, H. B. *Inorg. Chem.* **1962**, *1*, 111–122.
- (85) Wiberg, K. B. *Tetrahedron* **1968**, *24*, 1083.
- (86) Lever, A. P. B. *Inorganic Electronic Spectroscopy*, 2nd ed.; Elsevier: Amsterdam/New York, 1984.
- (87) Polavarapu, P. *J. Phys. Chem. A* **2005**, *109*, 7013–7023.
- (88) Varsano, D.; Espinosa-Leal, L. A.; Anfrade, X.; Marques, M. A. L.; de Felice, R.; Rubio, A. *Phys. Chem. Chem. Phys.* **2009**, *11*, 4481–4489.
- (89) This is an unusual isosurface in that one lobe of the four-lobe d_{yz} orbital above the plane of the corrin ring is bonding to an orbital on N24, and the other lobe above the plane of opposite sign is bonding to an orbital on N22.
- (90) Kornobis, K.; Kumar, N.; Wong, B. M.; Lodowski, P.; Jaworska, M.; Andruniow, T.; Ruud, K.; Kozlowski, P. M. *J. Phys. Chem. A* **2011**, *115*, 1280–1292.